

Silicon carbide absorption features: dust formation in the outflows of extreme carbon stars

Angela K. Speck, Adrian B. Corman, Kristina Wakeman & Caleb H. Wheeler

Department of Physics & Astronomy, University of Missouri, Columbia, MO 65211

speckan@missouri.edu

and

Grant Thompson

University of Kentucky, 600 Rose Street, Lexington, Kentucky 40506

ABSTRACT

Infrared carbon stars without visible counterparts are generally known as extreme carbon stars. We have selected a subset of these stars with absorption features in the 10-13 μm range, which has been tentatively attributed to silicon carbide (SiC). We add three new objects meeting these criterion to the seven previously known, bringing our total sample to ten sources. We also present the result of radiative transfer modeling for these stars, comparing these results to those of previous studies. In order to constrain model parameters, we use published mass-loss rates, expansion velocities and theoretical dust condensation models to determine the dust condensation temperature. These show that the inner dust temperatures of the dust shells for these sources are significantly higher than previously assumed. This also implies that the dominant dust species should be graphite instead of amorphous carbon. In combination with the higher condensation temperature we show that this results in a much higher acceleration of the dust grains than would be expected from previous work. Our model results suggest that the very optically thick stage of evolution does not coincide with the timescales for the superwind, but rather, that this is a very short-lived phase. Additionally, we compare model and observational parameters in an attempt to find any correlations. Finally, we show that the spectrum of one source, IRAS 17534–3030, strongly implies that the 10-13 μm feature is due to a solid state rather than a molecular species.

Subject headings: infrared: stars — stars: carbon — circumstellar matter — dust — stars: AGB and post-AGB

1. Introduction

1.1. Physical evolution of intermediate mass stars and their circumstellar shells

Stars between about 1 and $8 M_{\odot}$ will eventually evolve up the Asymptotic Giant Branch (AGB; Iben & Renzini 1983). Because of instabilities in their interior, AGB stars pulsate and throw off large amounts of mass from their surface (e.g., Vassiliadis & Wood 1993). This intensive mass loss produces a circumstellar shell of dust and neutral gas. Once the AGB star has exhausted its outer envelope, the AGB phase ends. At this point, the mass loss virtually stops and the circumstellar shell begins to drift away from the star. At the same time, the central star begins to shrink and heat up from ~ 3000 K until it is hot enough to ionize the surrounding gas, at which point the object becomes a planetary nebula (PN). The short-lived post-AGB phase, as the star evolves toward to the PN phase, is also known as the proto- or pre-planetary nebula (PPN) phase. During the ascent of the AGB, the velocity of the outflowing mass appears to be fairly constant (e.g., Huggins et al. 1988; Fong, Meixner & Shah 2003). Therefore the dust furthest from the star represents the oldest mass loss, while material closer to the star represents more recent mass loss. Towards the end of the AGB phase the increasing impact of the thermal pulse cycles leads to an increasing mass-loss rate (e.g., Vassiliadis & Wood 1993; Villaver et al. 2002a). Such an increase in mass-loss rate (dubbed the *superwind*) is necessary to explain the densities seen in typical PNe (Renzini 1981). Since the invocation of the superwind, many observations of AGB stars and post-AGB stars have supported this hypothesis (e.g., Knapp & Morris 1985; Wood et al. 1992).

1.2. Chemical evolution of AGB stars and their circumstellar shells

The chemical composition of the atmospheres of AGB stars is expected to change as these stars evolve, due to convective dredge up of carbon produced in the He-burning shell. The amount of carbon relative to oxygen (the C/O ratio) is critical in determining which types of dust and molecules are present around an AGB star. The formation of extremely stable CO molecules will consume whichever of the two elements is less abundant, leaving only the more abundant element available for dust formation. Stars start their lives with the cosmic C/O ratio of ≈ 0.4 and are therefore oxygen-rich. In about a third of AGB stars, enough carbon will be dredged up to make $C/O > 1$ and therefore carbon will dominate the chemistry around these stars, known as carbon stars. Carbon stars are expected to have circumstellar shells dominated by amorphous or graphitic carbon grains, which do not

have diagnostic infrared features. Another component of the dust shell around carbon stars, silicon carbide (SiC), does have an infrared spectral feature at $\approx 11\mu\text{m}$ and therefore has been of great interest to researchers seeking to understand the evolution of the dust shells and infrared features of carbon stars (Baron et al. 1987; Chan & Kwok 1990; Goebel et al. 1995; Speck et al. 1997; Sloan et al. 1998; Speck et al. 2005, 2006; Thompson et al. 2006).

1.3. Extreme Carbon Stars

As carbon stars evolve, mass loss is expected to increase. Consequently, their circumstellar shells become progressively more optically thick, and eventually the central star is obscured. Volk et al. (1992, 2000) christened such stars “extreme carbon stars”. These stars have also been dubbed “infrared carbon stars” (Groenewegen 1994), and “very cold carbon stars” (Omont et al. 1993). Extreme carbon stars are expected represent that small subset of carbon-rich AGB stars which are in the superwind phase, just prior to leaving the AGB. Because the superwind phase is short-lived compared to the AGB phase the number of extreme carbon stars is intrinsically small. Consequently, few of these objects are known. At present there are ~ 30 known extreme carbon stars in the Galaxy (Volk et al. 1992) compared to $\sim 30,000$ known visible carbon stars (Skrutskie et al. 2001).

van der Veen & Habing (1988) attempted to define a way to distinguish between oxygen-rich and carbon-rich AGB stars using IRAS color-color space, which was divided into subsections according to the properties of the dusty shells are these stars (see Table 1 of van der Veen & Habing 1988). This was further refined by Omont et al. (1993) who identified a population of very cold carbon stars using HCN and CO observations, and showed that the regions originally designated as extremely dusty O-rich AGB stars also contain a significant fraction of C-rich stars.

The refinement of the van der Veen & Habing (1988) color-color diagram by Omont et al. (1993) defined subdivisions of the seven zones in color-color space (see Fig. 1 in Omont et al. 1993). Cool carbon stars with high mass-loss rates (and little or no SiC emission) fall into regions III and IV, which had previously been assumed to define OH-IR stars (i.e. the oxygen-rich counterparts to extreme carbon stars). The numbered regions have been subdivided into smaller regions denoted by IIIa1, IIIa2, IIIb1 etc. A subset of the color-color space, covering parts of regions IIIa1c, IIIb2, IIIb2 and VIb is reproduced in Fig. 1 and includes our sample stars.

1.4. SiC absorption features

SiC has long been predicted to be present in carbon star circumstellar shells, beginning with condensation theories (Friedman 1969; Gilman 1969) and continuing with the prediction of a characteristic SiC $\sim 11\mu\text{m}$ spectral feature (Gilra & Code 1971) and then the observational discovery of an $\sim 11\mu\text{m}$ emission feature in many carbon star spectra (Hackwell 1972; Treffers & Cohen 1974). The effect of the evolving dust shell density structure on observed features, and particularly on the $\sim 11\mu\text{m}$ feature, have been discussed extensively (see review in Speck et al. 2005, and references therein). As the optical depth of the dust shell increases, self-absorption will diminish the $\sim 11\mu\text{m}$ feature and it will eventually be seen in net absorption. SiC self-absorption was found to be important in producing accurate radiative transfer models of extreme carbon stars (e.g. Volk et al. 1992), even though this previous work did not recognize SiC absorption features. These absorption features are rare and have mostly been ignored in discussions of evolutionary sequences in carbon star spectra. In fact the rarity of such absorption features led to the hypothesis that SiC becomes coated in carbon at high optical depths (e.g. Baron et al. 1987; Chan & Kwok 1990). However, meteoritic data and theoretical models do not support this hypothesis (see § 1.6 and § 3.4.1).

A few extreme carbon stars have been shown to have an absorption feature at $\sim 11\mu\text{m}$ which has been tentatively attributed to SiC. This feature was discovered in the “prototype” extreme carbon star AFGL 3068 (hereafter referred to as IRAS 23166+1655; Jones et al. 1978), and was re-examined by Speck et al. (1997), which also identified three additional extreme carbon stars with this feature. Clément et al. (2003) examined the absorption features of two of these extreme carbon stars (IRAS 23166+1655 and IRAS 02408+5458), and showed that their $11\mu\text{m}$ absorption features are consistent with β -SiC¹ nanoparticles. The broad absorption features of IRAS 19548+3035 and IRAS 21318+5631 (also discovered by Speck et al. 1997) were attributed to SiC absorption with an interstellar silicate absorption contribution (see also Groenewegen et al. 1996). This will be discussed further in § 4.6. The absorption features in the spectra of IRAS 19548+3035 and IRAS 21318+5631 were revisited by Clément et al. (2005) who suggested Si₃N₄ grains as the carrier. However, this hypothesis has been shown to be erroneous (Pitman, Speck & Hofmeister 2006).

The failure of the Si₃N₄ hypothesis led Speck et al. (2005) to suggest that amorphous SiC grains may be able to account for the breadth, structure and barycentric position of the observed broad 10-13 μm feature in IRAS 19548+3035 and IRAS 21318+5631. However, the dearth of amorphous presolar SiC grains seems to preclude this hypothesis (see § 1.6).

¹Silicon carbide exists in many (>70) different crystal structures, known as polytypes. See Speck et al. (1997); Daulton et al. (2003); Pitman et al. (2008) for a discussion of the polytypes of SiC.

An alternative explanation for this feature is molecular line absorption, however, currently available line lists are not sufficient to properly assess this hypothesis (see Speck et al. 2006, and references therein). One molecular candidate which has transitions in the correct wavelength range is C_3 (e.g. Zijlstra et al. 2006; Jørgensen et al. 2000), but the line lists are not readily available. Furthermore, C_3 is expected to be photospheric, rather than circumstellar, which probably precludes its detection in optically obscured stars. Moreover, the theoretical spectrum of C_3 from Jørgensen et al. (2000) shows a strong absorption close to the $\sim 5\mu\text{m}$ CO line, which is stronger than the $\sim 11\mu\text{m}$ feature. As will be seen in § 4.4, the spectrum of IRAS 17534–3030 does not show the $5\mu\text{m}$ absorption band and provides evidence that the observed absorption feature is not molecular in origin.

Though previous research has included the effects of SiC self-absorption (shown to be crucial to produce accurate models Volk et al. 1992; Speck et al. 1997, 2005), no work has been done to directly fit the apparent SiC absorption feature in radiative transfer models of extreme carbon stars.

1.5. Previous Radiative Transfer Models of Extreme Carbon Stars

Volk et al. (1992) performed radiative transfer modeling in order to match the Infrared Astronomical Satellite (*IRAS*; Neugebauer et al. 1984) Low Resolution Spectrometer (LRS) data for several of extreme carbon stars. They determined that the exact star temperature entered into the model was not important for the emerging spectra due to the very thick dust shells around extreme carbon stars (c.f. DePew et al. 2006; Speck et al. 2000). Their models used a fixed composition (a mixture of graphite and SiC), and a fixed dust condensation temperature. Groenewegen (1994) also performed radiative transfer modeling on a larger set of extreme carbon stars, but these models varied the dust condensation temperature. Again this was based on *IRAS* LRS data. Following up on this, Groenewegen (1995) modeled a large sample of carbon stars using amorphous carbon optical constants (Rouleau & Martin 1991), and assumed low dust condensation temperature in a fairly narrow range (650–900 K for the extreme carbon stars). Consequently the inner dust radius is larger than expected. Moreover the resulting models all have relatively low optical depths ($\tau_{11.3\mu\text{m}} < 2$). The optical depth for their IRAS 23166+1655 model was found to be $\tau_{11.3\mu\text{m}} < 1$, even though this star has an absorption feature at $11\mu\text{m}$. Groenewegen et al. (1998) remodeled these stars, again assuming relatively low dust condensation temperatures, with similar results.

Finally, Volk et al. (2000) used the improved spectral resolution of the the Infrared Space Observatory (*ISO*; Kessler et al. 1996) Short Wavelength Spectrometer (SWS; de Graauw et al. 1996) to examine five extreme carbon stars. In their modeling study, Volk et al. (2000) al-

lowed the optical depth and radial dust density distribution to vary; the resulting optical depths were relatively high (1.4-4.5 at $11.3\mu\text{m}$), and the density of the dust shell was found to increase rapidly towards the center. This increase was interpreted as evidence of an increasing mass-loss rate within the last few thousand years, consistent with the identification of extreme carbon stars as the final stage of AGB star evolution. While these models did include SiC opacity data, the $11\mu\text{m}$ absorption feature was not recognized and consequently no attempt was made to fit this feature in these models.

A summary of the parameters of previous models for extreme carbon stars with $11\mu\text{m}$ absorption features in our sample can be found in Table 1. Interestingly, all previous models assume relatively low inner dust temperatures. This will be discussed further in § 3.4.1. Furthermore, the modeled dust density distributions suggest a relatively slow increase in mass-loss rates ($1/r^x$, where $x \approx 2.25\text{--}3.0$).

In reality, dust shells are expected to have heterogeneities and anisotropies in their density structure as a result of pulsation-driven dust formation and the ensuing hydrodynamic turbulent effects (e.g. Woitke 2006). These dust formation models suggest that carbon star mass-loss is expected to be modulated on several timescales, especially that of the pulsation cycle. Furthermore Woitke (2006) has suggested that the dynamics in the dust-forming zones around carbon stars lead to inhomogeneous dust formation, producing fine scale structure in the density of the dust envelope. In addition, while pulsation shocks are predicted to have a strong effect on local conditions (e.g. Cherchneff 2006), this is not reflected in temporal changes in the IR spectra of carbon stars (Corman et al. 2008). As will be seen in § 4, the spatial scale of the heterogeneities is small and the timescale for pulsations is short compared to the timescales associated with even the thinnest dust shells. Moreover, the inhomogeneities are expected to be wiped out over time by the hydrodynamic interactions (Villaver et al. 2002a,b). Consequently, we do not consider these small scale structures in our models.

1.6. Meteoritic Evidence

The isotopic compositions of certain grains found in primitive meteorites indicate that they originated outside the solar system and are thus dubbed “presolar”. Dust grains from AGB stars are found virtually unaltered in these meteorites, demonstrating that these grains become part of the next generation of stars and planets (Clayton & Nittler 2004, and references therein). The precise physical characteristics of these meteoritic dust grains (e.g. sizes, crystal structures, compositions) can be used to help constrain the nature of the dust we see in our astronomical observations.

1.6.1. Presolar silicon carbide

Silicon carbide was the first presolar grain to be found in meteorites (Bernatowicz et al. 1987) and remains the best studied (Bernatowicz et al. 2006, and references therein). The most important findings of this work are (1) that most ($\sim 99\%$) of the SiC presolar grains were formed around carbon stars; (2) of the AGB SiC grains, $\approx 95\%$ appear to originate around low-mass carbon stars ($< 3 M_{\odot}$), based on nucleosynthesis models of isotopic compositions; (3) that all the SiC grains are crystalline (not amorphous); (4) that nearly all ($\approx 80\%$) are of the cubic β polytype, with the remainder comprising the lower temperature 2H polytype; (5) that with one exception, SiC grains have not been found in the cores of carbon presolar grains (unlike other carbides: TiC, ZrC, and MoC); and (6) that the grain size distribution includes both very small and very large grains ($1.5 \text{ nm} \rightarrow 26 \mu\text{m}$), with most grains in the $0.1\text{--}1 \mu\text{m}$ range. Single-crystal grains can exceed $20 \mu\text{m}$ in size. Observations of the $11 \mu\text{m}$ feature have been compared with laboratory spectra of various forms of SiC, and after some false starts it has now been attributed to β -SiC, matching the information retrieved from meteoritic samples (Speck et al. 1999; Clément et al. 2003). However, there are still some discrepancies between observational and meteoritic evidence (most notably related to grain size).

Prombo et al. (1993) found a correlation between grain size and the concentration of *s-process* elements in SiC grains taken from the Murchison meteorites. The Indarch meteorite presolar SiC grains yielded similar results (Jennings et al. 2002). In both cases, the smaller grains have higher relative abundances of *s-process* elements. This observation may be a result of different metallicity sources yielding different grain-size distributions (Lagadec et al. 2007, 2008). Alternatively, it may reflect an evolution in grain-size with dredge-up (Speck et al. 2005).

1.6.2. Presolar “graphite”

In addition to SiC presolar grains, carbon grains are also relatively abundant and well studied (see Bernatowicz et al. 2006, and references therein). Presolar carbon grains are usually referred to as “graphite” grains, but their structures are more complex than this name infers. Presolar graphite is found in two types of spherules classified according to their external morphologies as “onion-like” and “cauliflower-like”. In general the graphite spherules follow a similar size distribution to the SiC grains. However, the high-density grains ($\rho \approx 2.15 - 2.20 \text{ g cm}^3$) associated with AGB stars have a mean size of $2 \mu\text{m}$. In addition, the AGB presolar graphite spherules span a larger range of isotopic compositions than the SiC grains, possibly suggesting that they form at a wider range of times during the

AGB phase.

While the presolar SiC grains tend to be single crystals, the graphite grains regularly contain carbide grains. These carbides are enriched in *s*-process elements, indicative of formation around late-stage AGB stars. Many of the “onion-like” graphite grains have a core mantle structure in which the core contains disordered agglomerations of graphene² sheets and PAH³-like products, while the mantle is composed of well-ordered graphitic concentric shells. The graphene particles have a typical size of 3-4nm. The “cauliflower-like” graphite grains also have a concentric shell structure, but it is less well ordered, and is composed primarily of the disordered graphene. Whether “onion” and “cauliflower” graphites are formed in the same outflows is not known. Both types of grain contain the refractory carbides and both span the same range of isotopic compositions. Whether the “onion” or “cauliflower” grains are more representative of grains in the outflows of extreme carbon stars is not known. However, even the most disordered “cauliflowers” or “onion”-cores are still closer to graphite than glassy carbon in structure. The least ordered grains are still considered to be agglomerations of nano-crystalline grains, rather than truly amorphous (pers. comm. K. Croat).

1.6.3. Other presolar carbides

As discussed in § 1.6.1 and § 1.6.2, refractory carbides are found inside “graphite” grains but not in SiC grains. Furthermore, SiC is not one of the carbides found in “graphite” grains. The refractory carbides (TiC, ZrC, MoC and RuC) provide more constraints on the dust formation processes around carbon stars. In particular, the formation of “graphite” spherules with TiC nuclei limits the range of C/O ratios in which these grains could form to $1 \lesssim C/O \lesssim 1.2$. Meanwhile, the ZrC can form nuclei at higher C/O, but the value still needs to be less than two. This is consistent with the measured C/O ratios of Galactic carbon stars, which have an average of 1.15 and a maximum of 1.8 (Lambert et al. 1986)

²Graphene is basically a single sheet of graphitic material. If it is disordered, there are some heptagons and pentagons in place of the regular hexagonal carbon structure. Graphite is the 3-d structure.

³polycyclic aromatic hydrocarbon

1.7. Investigation

In the present work, we investigate a subset of extreme carbon stars, those which exhibit the $11\mu\text{m}$ absorption feature. Through radiative transfer modeling, we investigate the nature of these dust shells. We use theoretical models and meteoritic data to limit the parameter space and thus reduce the degeneracy within the model results. In addition, we look for correlations between observed parameters, such as those that define the $11\mu\text{m}$ feature (strength, position, etc) as well as mass-loss rates and expansion velocities associated with the dust shells. Finally we determine timescales associated with the dust shells.

2. Observations and Data Processing

We investigated 10 extreme carbon stars observed spectroscopically by the ISO SWS all of which show evidence for an $\sim 11\mu\text{m}$ absorption feature (see Table 2 and Figs. 2, 3,4 and 5). These sources were chosen by searching the ISO archive for spectra of extreme carbon stars listed in Volk et al. (1992) and selecting those with an apparent $11\mu\text{m}$ absorption feature. In addition, we used the color-color classification of “very cold” carbon stars by Omont et al. (1993) to identify further potential sources. Unfortunately most of the potential sources found in the color-color space (e.g. IRAS 17583-2291) were not observed by ISO SWS, and the IRAS LRS spectra are too low resolution and/or too noisy to be used in the present study. Four of our sources (IRAS 02408+5458, IRAS 19548+3035, IRAS 21318+5631, and IRAS 23166 +1655) were previously studied using ground-based observations and were found to be consistent with a self-absorbed SiC feature (Speck et al. 1997). Two of these sources needed an extra absorption component at $\sim 10\mu\text{m}$, which were attributed to interstellar absorption. As discussed in § 1.4, these have since been the source of some controversy (Clément et al. 2005; Pitman, Speck & Hofmeister 2006). Following the modeling efforts of Volk et al. (2000), Speck et al. (2005) identified IRAS 00210+6221, IRAS 06582+1507, and IRAS 17534–3030 as exhibiting an SiC absorption feature. The modeling of Volk et al. (2000) did not include SiC and did not attempt to fit the $11\mu\text{m}$ absorption. Thus, division of the observed spectra by their respective RT model spectra revealed the $11\mu\text{m}$ absorption feature. In this paper we present the discovery of three more potential SiC absorption features in ISO SWS spectra (IRAS 01144+6658, IRAS 03313+6058, and IRAS 22303+5950). These were discovered by searching the ISO archive for any extreme or “very cold” carbon stars as determined by their location in the IRAS color-color space. Those sources that fall within region III without OH maser emission were examined. The locations of the stars in our sample in *IRAS* color-color space (van der Veen & Habing 1988; Omont et al. 1993) are plotted in Fig 1. Interestingly, all sources except IRAS 19548+3035 plot along a line parallel

to and between the blackbody emission and the $B(T, \lambda, T) \times \lambda^{-1}$ emission lines.

The raw ISO data were extracted from the ISO data archive, and we used the Off-Line Processing (OLP) pipeline, version 10.1. Individual spectral sub-bands were cleaned of glitches (caused by cosmic ray particles) and other bad data sections. Next, they were flat-fielded, sigma-clipped (using the default values $\sigma = 3$) and rebinned to the final spectral resolution ($R = \Delta\lambda/\lambda$), which ranged from 200 to 700, depending on the scanning speed of the SWS grating during the observation (Leech et al. 2003). The final spectra are presented in Figure 2, which also shows the best-fitting⁴ blackbody continuum for each spectrum and the resulting continuum-divided spectra. The blackbody temperatures of the continua are listed in Table 3. The continuum-divided spectra clearly show an absorption feature in the 10-13 μm region, the basic parameters of which (barycentric position, peak-to-continuum ratio, full width half maximum; FWHM) are listed in Table 3. The excellent match between the overall spectrum and a single temperature blackbody suggests that we are seeing an isothermal surface within the dust shell. This represents the depth at which the shell becomes optically thick. The lack of extra emission at longer wavelengths suggests that any outlying dust is low enough in density to have an insignificant contribution to the overall emission.

In addition to the *ISO* SWS spectra, Fig 3, 4 and 5 shows the *IRAS* LRS spectra and the *IRAS* 12, 25, 60 and 100 μm photometry measurements. The difference in the flux levels between the *IRAS* and *ISO* data is not unexpected, since these stars are variable. However, the shape of the spectrum does not change significantly between the two observations, suggesting that changes in the stellar luminosity do not significantly impact the structure and composition of the dust shells.

In order to determine the cause of the 10-13 μm feature and the factors that govern its strength, width and position we have tabulated the barycentric position, feature-to-continuum ratio and equivalent width of the feature (Table 3). In addition, we have also tabulated where the barycenter of the SiC feature would be if the short wavelength side of the absorption is due to silicate (as has been postulated, see § 1.4). This, along with the feature-to-continuum ratio measured at 9.7 and 11.3 μm , can be found in Table 3.

2.1. The “30 μm ” feature

Another prominent spectral feature exhibited by our sample of extreme carbon stars is the so-called “30 μm ” feature. This feature is relatively common amongst carbon-rich

⁴Best fits are achieved by eye and proceed by examination of the continuum-divided spectra.

AGB stars, PPNe and PNe and was first discovered in Kuiper Airborne Observatory (*KAO*) spectra of carbon stars and PNe (Forrest et al. 1981). It has been widely attributed to magnesium sulfide (MgS; e.g. Goebel & Moseley 1985; Nuth et al. 1985; Omont et al. 1995; Begemann et al. 1994; Hony et al. 2002). Modeling this feature is beyond the scope of the present work, but will be investigated in follow-up modeling. Our models make no attempt to fit the “ $30\mu\text{m}$ ” feature.

3. Radiative Transfer Modeling

Radiative transfer modeling has been particularly useful in investigating extreme carbon stars (see § 1.5; Volk et al. 1992; Groenewegen 1995; Volk et al. 2000). We used the 1-D radiative transfer program DUSTY (Ivezic & Elitzur 1995; Nenkova et al. 2000), to determine the effect of dust shell parameters on the emerging spectra from carbon stars. In all cases, the central star was assumed to be at 3000 K (typical for an AGB star). Speck et al. (2000) and DePew et al. (2006) showed that changing this temperature by ± 1000 K did not significantly change the radiative transfer model’s spectra (c.f. Volk et al. 2000). For simplicity, dust grains are assumed to be spherical. While DUSTY can include other grain shapes, this expands parameter space to create more degeneracy between models and is beyond the scope of the present work.

3.1. Radial dust density distribution

We assume a radial dust density distribution of $1/r^2$ which would reflect a constant mass-loss rate. This choice is somewhat controversial and certainly needs justifying. Current dust formation models suggest that carbon star mass-loss is expected to be modulated on several timescales, especially that of the pulsation cycle (Woitke 2006, and references therein). Furthermore Woitke (2006) has suggested that the dynamics in the dust-forming zones around carbon stars lead to inhomogeneous dust formation, producing fine scale structure in the density of the dust envelope. While pulsation shocks are predicted to have a strong effect on local conditions (e.g. Cherchneff 2006), this is not reflected in temporal changes in the IR spectra of carbon stars (Corman et al. 2008). Previous models of extreme carbon stars have included steeper a density drop-off (see Table 1; Volk et al. 1992, 2000; Groenewegen 1995; Groenewegen et al. 1998), which is meant to represent the increasing mass-loss rate associated with the onset of the superwind phase. However, Villaver et al. (2002a,b) showed that the hydrodynamics in the circumstellar shell wipe out density structure and leave a shell with a $1/r^2$ density distribution. In addition Rowan-Robinson & Harris (1983) showed

that carbon star spectra can be well-fitted using such a density distribution.

In our models we assume that modulations in density have been wiped out or are unimportant in determining the spectrum at these high optical depths, as we are clearly seeing an outer dust shell surface. We also assume we are only detecting the dust that has formed since the onset of the superwind. We assume that there was a sudden increase in mass loss at some time in the last ~ 10000 years and that this mass-loss rate is now approximately constant, with small scale fluctuations being unimportant for dust properties. Consequently, the $1/r^2$ density distribution suffices. As will be seen in § 4, the impact of assuming a steeper the density distribution is to remove dependence on shell size, and thus remove the ability to out limits on timescales. If we were to adopt a $1/r^3$ density distribution, all the dust would effectively be contained close to the star and would reflect the total mass lost over only a relatively short period.

3.2. Modeling grain-size distributions

The issue of choosing a grain size distribution is interesting and certainly requires more discussion. Our initial modeling studies used an MRN distribution (i.e., $n(a)$ proportional to a^{-q} , where n is the number of the grains in the size interval $(a, a + da)$ and $q = 3.5; a_{min} = 0.005\mu\text{m}$; and $a_{max} = 0.25\mu\text{m}$; Mathis et. al 1977). This was chosen because as will become evident below, we do not actually know the grain size distribution and MRN is as plausible as any other. However, the MRN distribution was developed for interstellar dust where the balance of formation and destruction is different from AGB circumstellar environments. Dominik, Sedlmayr, & Gail (1989) suggested that the grain-size distribution created in the circumstellar environments of AGB stars has a steeper power law (i.e. a^5), while Kim, Martin & Hendry (1994, KMH) modified the MRN distribution to include an exponential fall-off term.

We should also consider the “observational” evidence for range and distribution of grain sizes in carbon star outflows. Meteoritic presolar SiC grains from carbon stars have a huge grain-size distribution, ranging for 1.5nm up to $26\mu\text{m}$, with the majority of grains ($\sim 70\%$) falling in the $0.3\text{--}0.7\mu\text{m}$ range (see Daulton et al. 2003; Bernatowicz et al. 2006; Clayton & Nittler 2004). Half the mass of the presolar SiC found in the Murchison meteorite is in grains larger than $0.6\mu\text{m}$ (Virag et al. 1992). Carbon presolar grains follow a similar grain size distribution to SiC (Bernatowicz et al. 2006). However, the sample may be biased in favor of large grains, which may be more apt to survive the journey through the ISM and incorporation into a solar system body.

Conventional theories of grain growth cannot produce the largest grains. Since AGB stars typically have mass-loss rates $< 10^{-5} M_{\odot} \text{ yr}^{-1}$ there should be an upper limit to the grain sizes of $\sim 0.1 \mu\text{m}$. However, this assumes an isotropic distribution of material. The existence of meteoritic titanium carbide (TiC) within presolar carbon grains necessitates density inhomogeneities in the gas outflows (c.f., inhomogeneities caused by turbulence in hydrodynamic models of carbon-rich dust formation regions; Woitke 2006). In addition, the grains must be $\lesssim 1 \mu\text{m}$ to produce the $11 \mu\text{m}$ feature, implying that there is a large population of small grains (but not necessarily precluding large grains). Constraints on grain size were also discussed by Martin & Rogers (1987) who found an upper limit to the grain size of $\sim 0.1 \mu\text{m}$ based on polarization measurements of the famous carbon star, IRC+10216. On the other hand, Groenewegen (1997) used polarization measurements to limit the grain size to $0.1 \leq a \leq 0.35 \mu\text{m}$ and suggested that very small grains ($< 80 \text{ nm}$) may not exist around carbon stars (however, smaller SiC grains are found in meteorites). Meanwhile, Jura (1994) argued the case for grains larger than $1 \mu\text{m}$ in the circumstellar shells of IRC+10216.

Towards the end of the AGB the onset of the superwind may lead to mass-loss rates as high as a few $\times 10^{-4} M_{\odot} \text{ yr}^{-1}$ (e.g. Hony et al. 2003) which could translate into larger grains (see e.g. Bernatowicz et al. 2006, and references therein). However, the relationship between the evolution of carbon stars and the consequent evolution of grain sizes in their circumstellar shells was discussed by Speck et al. (2005). They argued that the increased mass-loss rates at the end of the AGB phase lead to smaller, rather than larger grains as suggested by meteoritic evidence. Even the highest observed mass-loss rates cannot account for formation of titanium carbide (TiC) grains unless the distribution of material is not spherically symmetric and density enhancements exist (Bernatowicz et al. 2006). Such a distribution of material makes the concept of grain size distributions even more complex.

The range of grain sizes used in previous radiative transfer modeling attempts varies hugely. The IRC+10216 models of Griffin (1990) required grain sizes limited to $5 \leq a \leq 50 \text{ nm}$. Similarly Bagnulo, Doyle & Griffin (1995) required grains smaller than 50 nm . Groenewegen (1997) also modeled IRC+10216 and found that the spectrum was best fit using a single grain size of $0.16 \mu\text{m}$ (rather than a distribution of grain sizes). The single-grain size approach was also adopted by Volk et al. (2000) who assume a single grain size of $0.1 \mu\text{m}$. This is supported by the success of the early carbon star models of Rowan-Robinson & Harris (1983) who also used a single grain size ($0.1 \mu\text{m}$). However, since extreme carbon stars are expected to be the direct precursors for post-AGB objects, it may be more appropriate to consider the models of post-AGB stars. Such modeling efforts have found they need grains up to millimetre- or even centimetre- in size (e.g. Jura et al. 2000; Meixner et al. 2002). Meixner et al. (2002) used a KMH-like distribution with an effective maximum grain size of $200 \mu\text{m}$ (hereafter referred to as KMH200). Meanwhile, Szczerba et al. (1997) modeled a carbon-rich post-AGB

object with a power-law distribution of grains in the range $0.01\text{--}1\mu\text{m}$.

Given the range of possible grain sizes and distributions, it is difficult to know how best to model the dust. Groenewegen (1995) argued that the specific grain-size is not important as long as the grains are small enough that the absorption and scattering properties are independent of grain size. However, given the arguments for a population of large grains, limiting grains to smaller than $0.1\mu\text{m}$ is unrealistic.

In order to determine the effect of the choice of grain sizes on the model spectra we have generated models using five additional grains size distributions: 1) MRN-like with a steeper power law, i.e. $a_{min} = 0.005\mu\text{m}$, $a_{max} = 0.25\mu\text{m}$; $q = 5$ (as suggested by Dominik, Sedlmayr, & Gail 1989); 2) only $0.1\mu\text{m}$ -sized grains (as used or suggested by Volk et al. 2000; Rowan-Robinson & Harris 1983; Groenewegen 1995; Martin & Rogers 1987); 3) the dominant meteoritic grain sizes, i.e. $0.1\text{--}1\mu\text{m}$ only; 4) the standard KMH distribution (i.e. $n(a) \propto a^{-q}e^{a/a_0}$, $a_{min} = 0.005\mu\text{m}$, $a_0 = 0.2\mu\text{m}$; $q = 3.5$); and finally 5) KMH200: KMH with $a_0 = 200\mu\text{m}$. The results of this study are shown in Fig. 6, which shows the effect of changing the grain size distribution while keeping all other parameters constant.

If we examine the differences in the spectra generated by changing the grain-size distributions, this can be understood in terms of the absorption efficiency of the grains and breadth of the grain size distribution. Changing from our default grain size distribution (MRN) to a modified MRN-like distribution with a steeper power law drop off ($q = 5$) as suggested by Dominik, Sedlmayr, & Gail (1989) makes very little difference to the model spectral energy distribution (SED). Likewise, switching from MRN to KMH has little effect on the overall shape of the SED. That the MRN, $q = 5$ and the KMH models are so similar is because they are basically weighted towards the same small grains. While the weighting is different, the same-sized small grains dominate the SED. However, changing the size distribution to include larger dust grains as used in models of post-AGB stars (e.g. Meixner et al. 2002) has an major effect. The SED shifts to peak at much shorter wavelengths. This is because of the reduction in the number of small grains in order to include larger grains. The proportion of larger grains is small, but the removal of the smaller grains makes it possible for the stellar photons to penetrate deeper into the dust shell and provides a large population of warmer grains, resulting in a warmer SED. In both the KMH200 and $0.1\mu\text{m}$ cases there is a lack of very small grains which absorb a lot of stellar photons and change the temperature distribution (i.e. after the first layer of dust the temperature is lower, but if there are no small grains the stellar photons penetrate further.) Since size distributions similar to KMH200 are typically associated with long-lived dust disks, this particular distribution is not considered further.

For the meteoritic grain size distribution, the short wavelength side of the SED is similar

to the default (MRN) model, but now the SED is much narrower. This can be explained by the very narrow range of grain sizes. There are no very small grains that can be easily heated and thus the shorter wavelength emission seen in KMH200 does not occur, but the lack of small grains also allows deeper penetration of stellar photon leading to a narrower temperature distribution.

This grain size study suggests that for most adopted grain-size distributions, the resulting SEDs will be equivalent and we assume the MRN distribution as “generic”. However, the meteoritic grain-size distribution can narrow the overall SED. For this reason, our modeling efforts concentrate on the generic (MRN) and “meteoritic” grain size distributions, where the “meteoritic” is taken to be an extreme amongst the range of reasonable grain-size assumptions. The impact of choosing different grain size distributions and the implications of these differences for the potential errors in our models will be discussed in § 4. However, essentially, most grain-size distributions will yield the same results except for “meteoritic” and KMH200. In both cases changes in optical depth, inner dust temperature and/or relative geometrical shell thickness can be manipulated to fit the spectrum. There is a degeneracy in model fits due to the relationship between these three parameters that will be discussed in the next section. As will be seen in the § 4, the grain size effects cannot be ignored. In one source the need for “meteoritic” grain-size distribution is clear.

3.3. Parameter space investigated

In addition to grain sizes and radial density distribution, the variables investigated with DUSTY are the inner dust shell temperature (T_{inner}), optical depth (specified at $10\mu\text{m}$; $\tau_{10\mu\text{m}}$), dust composition, and the geometrical thickness of the dust shell, $\xi = R_{\text{out}}/R_{\text{in}}$, where R_{in} and R_{out} are the inner and outer radii of the dust shell, respectively. The optical constants for the dust components came from Pégourié (1988); Hanner (1998) and Draine & Lee (1984) for SiC, amorphous carbon and graphite, respectively. In nearly all cases it was possible to generate more than one model to fit the spectra, consequently we also investigate this degeneracy in parameter space and look for realistic ways to restrict it.

3.3.1. Degeneracies in radiative transfer modelling

There is a clear degeneracy in the models because of the relationship between certain parameters, e.g. optical depth and geometric shell thickness, or optical depth and the temperature at the inner edge of the dust shell. Ivezić & Elitzur (1997) discussed these degeneracies

and the relationship between the different input parameters in radiative transfer models, but we need to understand these relationship if we are to understand what our models mean.

The wavelength-dependent optical depth, τ_λ is defined by:

$$d\tau_\lambda = \rho(r)\kappa_\lambda dr \quad (1)$$

where $\rho(r)$ is the density of the absorbing/scattering particles (i.e. the dust grains) and κ_λ is the wavelength dependent opacity of the assemblage of particles along the line of sight.

$$\tau_\lambda = \int_{R_{\text{in}}}^{R_{\text{out}}} \rho(r)\kappa_\lambda dr$$

where R_{in} is the inner dust shell radius and R_{out} is the outer dust shell radius. While κ_λ is dependent on the density distribution of the grains, maintaining the size, shape and composition (and crystal structure) of the grains means that κ_λ will not change significantly. For simplicity we assume κ_λ remains constant. In our models we assume the density of the dust shell drops off as $1/r^2$ from the central star. In addition, our models specify the relative geometrical thickness of the dust shell as $\xi = R_{\text{out}}/R_{\text{in}}$. Thus we get:

$$\tau_\lambda = \kappa_\lambda \left[\frac{\xi - 1}{\xi R_{\text{in}}} \right] \quad (2)$$

The value of R_{in} is set by the values we input for the star's effective temperature and the inner dust radius (or condensation temperature, T_{inner}). If we know the temperature and luminosity of the star, we can use a $T(r) \propto r^{-\frac{1}{2}}$ temperature distribution to determine the relationship between T_{inner} and R_{in} and substituting into Eq. 2 we get:

$$\tau_\lambda = \sqrt{\frac{16\pi\sigma}{L_\star}} \kappa_\lambda T_{\text{inner}}^2 \left[\frac{\xi - 1}{\xi} \right] \quad (3)$$

Here we assume that the grains are blackbodies because they are largely carbon. Including the albedo would allow for a more accurate calculation, but this would depend on detailed dust parameters (like crystal structure), and the error incurred by our assumption is small (i.e. significantly less than an order of magnitude).

Therefore, according the Eq. 3, for a dust shell with constant relative shell thickness (ξ) the optical depth should increase with the square of the inner dust temperature. Alternatively, if the inner dust temperature is fixed, then increasing the relative shell thickness

should decrease optical depth a little (as $(\xi - 1)/\xi$). This latter effect becomes negligible for large geometric sizes.

3.4. Determining the Dust Condensation Temperature

3.4.1. Theoretical dust condensation models

As seen in the previous section, the value of the dust condensation temperature is a source of degeneracy on radiative transfer modeling. In order to reduce this degeneracy we turn to dust condensation theory to determine a theoretical dust condensation temperature (i.e. T_{inner}) that is appropriate for our stars.

As discussed in § 1.6, many presolar grains can be attributed to carbon stars and are valuable resources for investigation of dust formation regions. For example, in presolar grains titanium carbide (TiC) is found in the center of carbon (C) grains from AGB stars, but only one SiC grain has been found coated in carbon (Clayton & Nittler 2004; Bernatowicz et al. 2006). Consequently there have been many studies of the theoretical condensation sequence in Galactic carbon stars in attempts to constrain the physical parameters of the dust condensation regions. These studies showed how the condensation sequence of C, TiC and SiC is dependent on various parameters, most notably C/O ratio and gas pressure⁵ (Lodders & Fegley 1995; Sharp & Wasserburg 1995). Sharp & Wasserburg (1995) argued that if carbon forms at a higher condensation temperature, closer to the star than SiC, there is a significant decrease in the amount of carbon available in the gas, and thus SiC and C do not form simultaneously, resulting in naked SiC grains. Therefore, for Galactic sources, the condensation sequence in the majority of carbon stars should be TiC — C — SiC, in order to produce the coated TiC grains and uncoated (naked) SiC grains seen in the meteoritic presolar grains samples. Observational evidence for naked SiC grains is discussed by Speck et al. (2005). Sharp & Wasserburg (1995) argued that from kinetic and stellar model considerations, dust grains should form in the pressure range $2 \times 10^{-7} < P < 4 \times 10^{-5}$ bars⁶.

Lodders & Fegley (1995) also modeled the effect of C/O and pressure on the condensation sequence in carbon stars, as well as the effect of *s*-process and nitrogen abundances. They also briefly discuss the effect of metallicity. The general trends in condensation tem-

⁵Gas pressure is a measure of the mass-loss rate (\dot{M}) convolved with the photospheric temperature (T_{\star}) and outflow velocity (v_{exp}).

⁶The expected range of gas pressures in the dust formation zone for O-rich AGB stars in the LMC is 10^{-7} bars $\lesssim P \lesssim 10^{-4}$ bars (Dijkstra et al. 2005)

peratures are: (1) all condensation temperatures decrease as the gas pressure decreases; and (2) At $C/O > 1$ the condensation temperature of graphite increases with C/O (for a given pressure and otherwise constant composition).

Figure 7 shows how the condensation temperature of carbon and SiC vary with the gas pressure in the dust condensation zone. For the range plotted carbon always forms first from a cooling gas. Very high pressures are required for SiC to form before carbon. For solar metallicity and $C/O = 1.05$, SiC forms before carbon for $P \geq 3.4 \times 10^{-5}$ bars. As C/O increases, the minimum pressure required to form SiC first increases. Above $C/O \sim 1.5$ carbon always forms before SiC. The exact C/O ratio at which the carbon forms before SiC depends on pressure. Therefore, in order to account for observations of SiC features in the Galaxy, and the presolar grain record, we can restrict the P - C/O space such that, for low C/O the gas pressure must remain low, but for higher C/O the pressure can be higher. This can be used to constrain the dust forming environment around Galactic carbon stars.

Studies of carbon star spectra in the Galaxy and the Magellanic Clouds have lead to different interpretations with respect to the condensation sequence. Lagadec et al. (2007) argued for a sequence in which SiC forms before C in the Galaxy, whereas SiC and C form together in the Large Magellanic Cloud (LMC) and the sequence is reversed (C, then SiC) in the Small Magellanic Cloud (SMC). However, they also suggest that the change in the strength of the features is due to the lower number of Si atoms available for SiC formation. The proposed Galactic condensation sequence is at odds with both the models and the meteoritic evidence. Leisenring et al. (2008) support the condensation sequence in which C forms before SiC for the Galactic carbon stars, while finding that the Magellanic Clouds tended to form SiC first, followed by simultaneous condensation of SiC and C. Speck et al. (2006) used the Lodders & Fegley (1995) model to explain an unusual LMC carbon star spectrum, which suggests that the condensation sequence is sensitive to both metallicity and mass-loss rate.

3.4.2. *P-T space in the condensation zone around extreme carbon stars*

In order to constrain the input parameters to our model we need to be able to determine the pressure-temperature space in the dust condensation zone. For a mass-losing star with a mass-loss rate \dot{M} and an expansion velocity of v_{exp} , the density ρ of the circumstellar shell at a radius r is given by:

$$\rho = \frac{\dot{M}}{4\pi r^2 v_{\text{exp}}}$$

If we know the temperature and luminosity of the star and the composition of the outflowing material we can combine this information with the Ideal Gas Law and a $T(r) \propto 1/\sqrt{r}$ temperature distribution to determine the gas pressure at the condensation radius, where the condensation radius is the distance from the star where the gas has the condensation temperature (T_{cond}).

For simplicity, the solid and gas phases are assumed to be at the same temperature. While this is clearly a simplification (e.g. Chigai & Yamamoto 2003), the temperature difference is small compared to the difference needed to significantly affect dust formation. We assume that most of the outflowing material is atomic hydrogen. In fact it will probably be a mixture of atomic and molecular hydrogen (H_2) since H_2 forms around 2000 K and the temperature in the outflow is decreasing from the stellar surface temperature of ~ 3000 K to the dust condensation temperature in the 1000–1800 K range. An entirely molecular hydrogen gas would halve the gas pressure compared to the atomic gas. However, we also assume published CO outflow velocities, which reflect the speed of the outflowing material after radiation pressure acceleration. Adopting the pre-dust-formation outflow speed ($\lesssim 5$ km/s), would increase the pressure. Thus using published values for our sample stars’ luminosities, mass-loss rates and expansion velocities, we can estimate where their dust condensation zones fall in P–T space.

3.4.3. Comparison of P–T space for dust condensation models and sample stars

Figure 7 shows how the P–T space for the dust condensation zone for our target stars compares to condensation models in P–T space. It is clear the pressure is never high enough for SiC to form before carbon. Since our sample stars are expected to be the carbon stars with the highest mass-loss rates, it implies that this NEVER happens in Galactic carbon stars. This agrees with the meteoritic evidence which suggests that SiC does not get coated in carbon and supported the idea that variations in the strength of the SiC feature are related to self-absorption.

The dust condensation temperature is dependent on the pressure in the gas from which the dust forms. In addition, the P–T space occupied by the target sources suggests that carbon grains will form at temperatures $\gtrsim 1600$ K. If the C/O is very high, then graphite could form as high as ~ 1800 K. However, Galactic carbon stars for which the C/O ratios have been measured show that it is in the range 1 to 1.8, with a mean C/O ratio of ~ 1.15 (Lambert et al. 1986; Olofsson et al. 1993a,b). The precise C/O for our sample is not known, but even low C/O stars yield $T_{\text{cond}} \gtrsim 1550$ K (see Fig. 7). Previous models of carbon stars have assumed much lower inner dust temperatures. The pressures and temperatures in the

gas around these stars meet the criteria for forming carbon dust at $T_{\text{cond}} \gtrsim 1600$ K, (precise temperature depends on the C/O ratio). Therefore it should form at these high temperatures.

Once dust starts to form, the radial temperature profile will change due to absorption of starlight by dust grains. Therefore, we use the comparison above only to determine the inner dust radius. Using radial temperature profiles from our models we show that the temperature drops significantly more rapidly than $1/\sqrt{r}$ (see Fig. 7), which suggests that the next condensate (SiC) forms fairly close to the inner dust radius and thus mitigates the problem with DUSTY that the grains are assumed to be co-spatial. Indeed the models show that the temperature in the dust shell drops to the SiC formation temperature at $\sim 1.3R_{\text{in}}$ for all cases, which is small compared to the shell thickness, even for the thinnest shells.

3.5. Constraining Dust Composition

Since our stars are carbon-rich, we limit the models to only including carbonaceous species such as graphite, amorphous carbon and silicon carbide. The choice of carbon grains is equivocal. We do not know whether the grains composed mostly of carbon are glassy, poly-nanocrystalline or well-ordered. The meteoritic presolar “graphite” grains suggest that circumstellar dust can contain either well-ordered graphite or poly-nanocrystalline-graphene grains. It should be noted, however, that even the disordered graphene sheets are considered to be more graphitic than amorphous.

Amorphous carbon essentially consists of a mixture of sp^2 (graphite-like) and sp^3 (diamond-like) carbon bonds. On heating, sp^3 bonds tend to convert to sp^2 bonds, thus graphitizing the amorphous carbon, but it will remain dense like the amorphous phase (2.8 g/cm^3 Comelli et al. 1988; Saada 2000; Kelires 1993). At ~ 1300 K the fraction of graphitic bonds is $\sim 90\%$. Comparison of the gas pressure in the circumstellar outflows to graphite formation temperature in § 3.4.3 shows that graphite should be able to form at temperatures significantly above 1300 K. Even if solid state carbon forms as a chaotic solid, at these temperatures it will quickly anneal to a graphitic form. Consequently, we argue that graphite is the better choice of carbonaceous material for modeling extreme carbon star dust shells.

The limitations of the use of the Pégourié (1988) data are discussed in Pitman et al. (2008). Clearly, this data cannot produce the broad absorption feature seen in the observations. However, we can use the relative changes in composition from star to star as a guide to understanding why these stars have the features we see.

4. Radiative Transfer Modeling Results

The results of the radiative transfer modeling can be seen in Fig. 8, 9 and 10. The parameters used in each case can be seen in Table 5. For each source, we have produced models using both MRN (generic) and “meteoritic” (extreme) grain size distributions.

4.1. The effect of grain-size distribution

Table 5 shows the model input parameters for both grainsize distributions. In all cases switching from MRN to “meteoritic” grainsizes leads to the need for increased SiC component (compared to graphite), typically requiring a three- or fourfold increase in the SiC fraction.

There are other general trends including the need for decreased optical depths ($\tau_{10\mu\text{m}}$) and increased geometric shell thickness. However, these trends do not hold for all objects. In the cases of IRAS 00210+6221 and IRAS 06582+1507, the only difference in parameters between the different grain size models is the fraction of SiC. IRAS 01144+6658 is the only source for which optical depth was increased and shell thickness was decreased in the “meteoritic” model.

4.2. Dust Shell Thicknesses

As discussed in § 3.3.1, there is a degeneracy between relative shell thickness, inner dust temperature and optical depth. The inner dust temperature variability has been limited to 1550–1800 K by theoretical considerations (see § 3.4.1). It is possible to tweak parameters such as shell thickness, inner dust temperature and optical depth and get almost identical models. Fig. 11 shows two almost identical model spectra for IRAS 23166+1655 with different inner dust temperatures, optical depths and shell thicknesses. However, reducing the inner dust temperature merely requires reduction of the optical depth. While increasingly geometrically large dust shells can be accommodated by decreasing optical depth (see Eq. 3), at some point, this also breaks down, as it leads to a significant population of colder grains which emit too much at long wavelengths. In this way we can use the models to place to an *upper limit to the shell thickness*. Table 4 lists the published expansion velocities for our extreme carbon stars. From the model parameters, the physical value for R_{out} can be calculated, which gives the physical size of the dust shell. Since the models give an upper limit to the shell thickness, this upper limit to R_{out} together with the expansion velocity (v_{exp}) was used to calculate the time since the outermost edge of the shell was ejected from the star. The resulting ages of the dust shells are listed in Table 6.

As can be seen in Fig. 6, it is possible to accommodate thick shells, if we assume a much lower T_{inner} (1000 K), and assume that the dust grain are composed of amorphous rather than graphitic carbon, but these parameter values are precluded by the theoretical constraints on T_{inner} and composition/crystal structure discussed above. Clearly, since our constraints are theoretical, they may change as hypotheses are refined.

The timescales for increased mass-loss are model dependent. As can be seen in Table 5 using a “meteoritic” grain size distribution generally requires a geometrically thicker shell, as well as lower values for $\tau_{10\mu\text{m}}$ and higher percentages of SiC. However, timescales associated with our dust shells are always very short (less than a few thousand years) regardless of grain-size distribution. Moreover, our timescales are consistent with those derived for the “superwind” seen in post-AGB objects (e.g. Skinner et al. 1997; Meixner et al. 2004). These timescales are too short to be associated with the theoretical superwind (e.g. Vassiliadis & Wood 1993), which is expected to last up to $\sim 10\%$ of the duration of the thermally-pulsing AGB phase. However, if we compare the number of extreme carbon stars to the total number of carbon stars in the Galaxy, we find that extreme carbon stars constitute only $\sim 0.1\%$ of the total C-star population. The thermally pulsing AGB phase is expected to last $\sim 10^6$ years, and the time a star spends as a C-stars is even shorter (e.g. Lagadec et al. 2007). Consequently, we might expect the dust-obscured phase to only last $\sim 10^3$ years. This is consistent with the model timescales, although the MRN-models still appear to have very short timescales. Lagadec & Zijlstra (2008) suggested that the trigger for the superwind is a combination of luminosity and carbon abundance. Although the duration of the C-star phase maybe be $\sim 3 \times 10^5$ years, for much of this time, a C-star will be below the critical carbon abundance required to drive the superwind and obscure the star.

How does the extreme carbon star phase fit into the broader C-star evolution? Many, if not most, carbon-rich post-AGB stars showed marked axisymmetric morphologies (Meixner et al. 1999; Waelkens & Waters 1999; Sahai 2004; Soker & Subag 2005). The extreme carbon stars are expected to be the direct precursors of these objects (e.g. Skinner et al. 1998), but presently show little evidence for axisymmetry⁷. The cause and timing of this axisymmetric structure is not known, but is believed to occur at the very end of the AGB phase. Dijkstra & Speck (2006) showed that significant axisymmetry is not expected to develop until the last few tens or hundreds of years of the superwind phase. The onset of axisymmetry also leads to an optically thicker toroid of dust, as the circumstellar shell becomes equatorially enhanced. We suggest that the very short timescales associated with our model results may indicate that the extreme AGB stars are in the process of developing axisymmetry, but

⁷one would expect to see more near-IR emission in the spectrum of strongly axisymmetric objects due to scattering of starlight escaping in the bipolar axis direction.

that this has not developed to the point of allowing large amounts of NIR scattered light into the spectrum.

4.3. Dust Shell Density Distribution

In § 3 we argued the case for maintaining a dust density distribution that follows a $1/r^2$ law. However, it has been argued that the increasing stellar luminosity and the onset of the superwind phase should give rise to a steeper density drop-off.

Following the same arguments as shown in § 3.3.1, giving rise to Eq. 3 we can derive an equation in which the exponent of the density power law is a variable. This gives us the relationship between the optical depth (τ_λ), inner dust temperature (T_{inner}), relative shell thickness (ξ) and the exponent of the density power law (x):

$$\tau_\lambda = \kappa_\lambda \left[\frac{\xi^{x-1} - 1}{(x-1)\xi^{x-1}} \right] \left(\sqrt{\frac{16\pi\sigma}{L_\star}} T_{\text{inner}}^2 \right)^{x-1} \quad (4)$$

where κ_λ is the wavelength dependent opacity of the assemblage of particles along the line of sight; L_\star is the luminosity of the star; and σ is the Stefan-Boltzmann constant.

As an example of the effect this, we assume the exponent, $x = 3$ (which is the highest value in the previous models). In this case, the relative shell thickness dependence dwindles, and the optical depth is essential strongly dependent on the inner dust temperature only. Since the previous models have severely underestimated the inner dust temperature, they have also underestimated the optical depth (which may explain Groenewegen 1995).

The lack of dependence on shell thickness at $x > 2$ leads to a situation where most of the dust is essentially confined to a region close to the star and the outer dust becomes negligible, and so this confinement to the inner region is effectively the same as our assumption that there was a sudden increase in mass loss in the recent past. However, we attempted to model our sources with a $1/r^3$ radial density distribution and found that we cannot match the shape of the SED without restricting the geometrical shell thickness. Using the $1/r^3$ radial density distribution with the MRN grain-size distribution and $R_{\text{out}}/R_{\text{in}} \gtrsim 20$ produces a SED that has too much emission longwards of $\sim 20\mu\text{m}$. Therefore, even if the radial density distribution is indicative of a steep increase in mass-loss rate the shells still need to be geometrically thin, and the shell thickness and percentage of SiC needed are essentially the same as for the $1/r^2$ models (see Fig. 11 for an example.) If the “meteoritic” grain-size distribution is used in conjunction with a $1/r^3$ drop-off, the observed SED cannot be matched. The model SED becomes too narrow, and increasing the outer dust-shell radius

does not help.

4.4. IRAS 17534–3030

IRAS 17534–3030 is exceptional amongst the present sample of extreme carbon stars, and certainly requires more discussion. As can be seen in the flux-calibrated and continuum-divided spectra in Fig. 2, IRAS 17534–3030 does not exhibit the usual molecular absorption bands around $13.7\mu\text{m}$ (due to C_2H_2) and shortwards of $\sim 8\mu\text{m}$ (due to both C_2H_2 and HCN), which are present in the other sample sources. Its $11\text{--}13\mu\text{m}$ feature is intermediate between the narrow feature exemplified by IRAS 23166+1655 and the broad feature exemplified by IRAS 19548+3035, indicating that at least some of whatever substance causes the broadening is present around IRAS 17534–3030. One of the suggested carriers for the short wavelength broadening of the $10\text{--}13\mu\text{m}$ absorption feature is C_3 (Zijlstra et al. 2006). However, C_3 is expected to be photospheric, rather than circumstellar, which probably precludes its detection in optically obscured stars. Moreover, the theoretical spectrum of C_3 from Jørgensen et al. (2000) shows a strong absorption close to the $\sim 5\mu\text{m}$ CO line, which is stronger than the $\sim 11\mu\text{m}$ feature. The spectrum of IRAS 17534–3030 does not show this $5\mu\text{m}$ absorption band. This, together with the lack of other molecular absorption feature provides evidence that the broadening of the $10\text{--}13\mu\text{m}$ feature is not molecular in origin.

In addition to the lack of molecular absorption in its spectrum, IRAS 17534–3030 is unique in another way: it cannot be modeled with the MRN grain-size distribution. Modeling of this source requires the “meteoritic” grain-size distribution because of its narrow SED. Whereas our other sources can be fitted with either MRN or “meteoritic” grains, IRAS 17534–3030 cannot.

4.5. Impact of the dust condensation temperature

The increase in the inner dust temperature from $\lesssim 1000\text{ K}$ in previous models up to $\gtrsim 1600\text{ K}$ decreases the inner dust radius significantly. Consequently the flux of energy from the star hitting the inner dust radius is increased, leading to a greater acceleration and consequently a more effectively dust-driven wind. If graphite is formed by annealing of amorphous carbon, the grain density should remain high (with $\rho=2.8\text{g/cm}^3$) and the increased acceleration is entirely due to increases flux of stellar photons. However, if graphite forms directly, rather than by annealing of amorphous carbon, the radiation pressure effect is further enhanced, because graphite grains generally have a lower density than amorphous carbon.

Assuming $0.1\mu\text{m}$ -sized grains, the acceleration felt by graphite grains (with $\rho=2.2\text{g/cm}^3$; c.f. meteoritic presolar grains; see § 1.6.2) at $T_{\text{inner}} = 1800\text{K}$ is 13 times greater than the acceleration felt by amorphous carbon grains (with $\rho=2.8\text{g/cm}^3$) at $T_{\text{inner}} = 1000\text{K}$.

4.6. Correlations between observed and model parameters

In the course of this investigation we have compiled a large number of parameters for these stars. For instance, Table 3 lists the peak position, peak strength, FWHM and equivalent width of the $\sim 11\mu\text{m}$ absorption feature. Table 4 lists the published mass-loss rates, luminosities and expansion velocities for our sample stars.

In order to understand the physical conditions that give rise to the observed $11\mu\text{m}$ absorption feature, we have sought correlations between various parameters associated with the sample stars (as found in Table 3, 4, 5). We have looked for correlations between each of the following: mass-loss rate (from CO observations); expansion velocity (from CO observations); stellar luminosity; strength of the observed absorption; FWHM of the absorption; barycentric position of the absorption; equivalent width of the absorption; and model parameters.

Loup et al. (1993) showed that, for low mass loss rates there is a simple relationship between the [25]-[12] color and mass-loss rates. This breaks down at mass-loss rates $\gtrsim 10^{-5}\text{M}_{\odot}\text{yr}^{-1}$. It has been suggested that such high mass-loss rate stars are CO-emission deficient due to either saturation effects, low kinetic temperatures or possibly dramatic recent increases in mass-loss. If we extrapolate the trends from low mass-loss rates to determine mass-loss rates from the [25]-[12] color we find that these objects should have a mass-loss rate in excess of $10^{-4}\text{M}_{\odot}\text{yr}^{-1}$, consistent with the high modeled optical depths. Because of this relationship, we sought correlations between the various observed and modeled parameters and the [25]-[12] and [60]-[25] colors. This search yielded only one correlation: between the [60]-[25] colors and the dust mass-loss rate from previous models. It is possible that a better correlation may be found using the *Manchester Method* i.e. the [6]-[9] color (e.g. Sloan et al. 2006; Zijlstra et al. 2006), however, we suspect that the lack of correlation arises because of the intrinsic degeneracy in the modeling.

In § 1.4 and § 2 we discussed the possibility that the broadening of the $10\text{--}13\mu\text{m}$ feature might be due to silicate dust. With this in mind, we re-measured the position and strength of the $11\mu\text{m}$ feature assuming that the short wavelength wing is due to silicate. This involved measuring the feature-to-continuum strength at 9.7 and $11.3\mu\text{m}$. These data are tabulated in Table 3 and were also included in the investigation of correlations between parameters.

One pair of parameters that yielded a correlation were the best-fit blackbody temperature and the model optical depth, which is demonstrated in Fig 12. This correlation occurs whether we assume MRN or “meteoritic” grainsizes. Since there is a relationship between the optical depth and shell thickness, this correlation seems to support models validity.

In addition to this relationship between the modeled optical depth and the best-fit blackbody temperature, we found two other parameters that the optical depth correlates with: modeled percentage of SiC in the dust shell; and the calculated timescale of the obscuring dust. In both cases, these correlations only hold for the generic (MRN) grain-size distribution models. (shown in Fig. 13). The correlation between optical depth and percentage SiC is such that lower optical depths require more SiC. This in turn suggests that as mass-loss rates increase, the SiC component dwindles. This can be interpreted in two ways: (1) at these high mass-loss rates SiC gets coated by carbon; and (2) increased mass-loss rates are associated with higher C/O ratios; carbon is enriched but not silicon, and thus more carbon grains can be made, but not more SiC grains. The first option seems unlikely in light of meteoritic evidence (§ 1.6) and theoretical condensation models (§ 3.4.1). However, it is possible that there is a metallicity effect in play. The presolar grains were formed prior to the formation of the solar system, and thus their source stars may have had lower metallicities. Speck et al. (2006); Leisenring et al. (2008) argued that coating of SiC grains is more likely in lower metallicity environments, and thus it is difficult to see how the higher metallicity objects we are now witnessing could have carbon-coated SiC grains. However, Leisenring et al. (2008) argued that SiC grains form the nucleation seed for MgS, which may explain this correlation. The second option may be logical if outflows are dust driven. If more carbon grains can form, the radiation pressure driving the outflow is more effective.

The second optical depth correlation is with the calculated timescale (also shown in Fig. 13 and again, only for the MRN grain-size distribution). In this case, the timescale for the dustshell increases with optical depth. The oldest shells have the highest optical depth. This may simply be due to the pathlength dependence of optical depth (see Eqn. 1), since τ depends on the geometric size of the dust shell the oldest shells should have the largest optical depth. However, this should also lead to a correlation between model dust shell thickness and optical depth. No such correlation exists. Another interpretation is that older stars have higher mass-loss rates, and thus denser dust shells and higher optical depths. However, this assumes the stars all had the same initial mass. This apparent correlation is not strong, and does not holds for “meteoritic” grains. Consequently, we will not attempt to place too much importance on it.

There is no correlation between the strength of the $9.7\mu\text{m}$ absorption and that at $11.3\mu\text{m}$,

implying that the carriers of these features may not be related. Furthermore, there is no correlation between the $9.7\mu\text{m}$ strength and distance to the object, which leads us to suggest that the cause is not interstellar. Obviously there is a strong correlation between the strength of the $9.7\mu\text{m}$ absorption and the barycentric position of the feature, indicating that this is the cause of the broadening.

The most interesting correlations are between the “isolated” $11.3\mu\text{m}$ feature (i.e. the residual feature after taking silicate absorption into account) and the fitted blackbody temperature. There is a correlation both between the SiC barycentric position and the blackbody temperature and between the $11.3\mu\text{m}$ feature-to-continuum ratio (i.e. SiC feature strength) and the blackbody temperature (both shown in Fig. 12).

The position of the SiC absorption feature moves to shorter wavelengths for higher blackbody temperatures while also becoming weaker. This can be understood as being the result of more absorption occurring when the surface we see is at a lower temperature, which is associated with longer wavelength absorption.

We can interpret this result in terms of the self-absorption scheme described by Speck et al. (2005). The shifts in wavelength were attributed to a changes in grain size. However, the weaker absorption and warmer blackbody temperatures associated with the shortest wavelength peaks is the opposite trend to that described by Speck et al. (2005). Following their scheme, this would imply that the weakest absorption is associated with the largest SiC grain. The problem with interpreting this observation is that we do not know the C/O ratios for these stars. While C/O does not affect the SiC condensation temperature, it will affect the graphite condensation temperature. As seen in Fig 11, we can reduce the inner dust temperature and compensate by decreasing both the optical depth and the shell thickness. This would also change the depth into the shell at which the SiC forms. It is also possible that the shift in position is due to incomplete subtraction of the silicate contribution. Further studies are ongoing, but are beyond the scope of the present work.

The assumption that there is a silicate contribution to the spectrum raises several questions. Identifying the source of the $9.7\mu\text{m}$ contribution to the absorption feature remains beyond the scope of the present paper, but, needless to say, if it is silicate, the specter of dual chemistry would require seriously rethinking our current models of dust formation around carbon stars. Lodders & Fegley (1999) suggested that silicates could form around carbon stars, and indeed silicate carbon stars exist. It is possible that the feature may be attributable to some form of hydrogenated amorphous carbon, which has been postulated as the source of an $\sim 9\mu\text{m}$ emission feature in optical thin carbon star spectra (see Thompson et al. 2006, and reference therein).

No additional correlations were found. The lack of correlation between most of the observable or modeled parameters echoes the results of Thompson et al. (2006), who found that there are no trends in the parameters associated with $11\mu\text{m}$ emission feature in visibly observable carbon stars. This suggests that even amongst the extreme carbon stars, variations in C/O, *s*-process and nitrogen enhancements make discernment of the physical properties associated with the $11\mu\text{m}$ feature very difficult.

5. Conclusions

We have presented three previously unrecognized SiC absorption features in the spectra of extreme carbon stars. Together with the seven known SiC absorption stars, this brings the total of known extreme carbon stars with SiC absorption features to ten.

Previous radiative transfer models of extreme carbon stars utilized relatively low condensation temperatures. Here, theoretical condensation models have been used to justify much higher condensation temperatures. In addition, our models use graphite instead of amorphous carbon, because of the preferential formation of graphite at higher temperature and the meteoritic evidence. Both the higher condensation temperature (through a decrease in the inner radius of the dust shell) and to a smaller extent the use of graphite will greatly increase the acceleration felt by the dust grains in the shell relative to parameters used in previous research.

We have shown that grain-size issues cannot be ignored in the production of models that accurately fit the observed spectra of extreme carbon stars. The size distribution that is needed is not clearly defined because of the inherent degeneracy in radiative transfer modeling. Meteoritic grain-size distributions are as valid as other size distributions with the advantage of being model independent. However, they may underestimate the contribution from small grains.

With the exception of IRAS 17534–3030, all sample stars could be modeled with either the generic (MRN) or “meteoritic grain-size distribution IRAS 17534–3030’s narrow SED required the use of the “meteoric” distribution. Furthermore, there is no evidence for any molecular absorption in its spectrum. Because the $11\mu\text{m}$ feature is still present in the absence of the other molecular features, it supports the attribution of this feature to a solid state carrier.

The various parameters compiled in the course of this research (both through radiative transfer modeling and from observations) have been compared in order to identify any correlations, with the result that the cause of differences in the spectra cannot be attributed to

mass-loss rate or gas pressure in the dust condensation zone. In fact the paucity of correlations between parameters echoes the results of Thompson et al. (2006) and suggests that even amongst the extreme carbon stars, variations in C/O, *s*-process and nitrogen enhancements make $11\mu\text{m}$ a poor probe of the details of dust shell parameters.

The timescales associated with the heavy mass-loss experienced by these extreme carbon stars are very short (tens to hundred of years) and are not consistent with timescales for the superwind. This indicates that the heavy mass-loss phase of carbon stars is not a direct result of thermal pulse (although thermal pulses may be the root cause).

This work is supported by NSF AST-0607341. We are very grateful to the referee, Albert Zijlstra, for his comments which have significantly improved this paper. Kevin Volk is also thanked for helpful advice on this paper.

REFERENCES

- Amari S., Jennings C., Nguyen A., Stadermann F.J., Zinner E., Lewis R.S., 2002, Lunar Planet. Sci. Conf., 33, 120
- Bagnulo, Doyle & Griffin, 1995, A&A, 301, 501.
- Baron, Y., de Muizon, M., Papoular, R., & Pégourié, B. 1987 A&A, 186, 271.
- Begemann, B., et al., 1994, ApJ, 423, L71.
- Bernatowicz, T., Fraundorf, G., Ming, T., Anders, E., Wopenka, B., Zinner, E., Fraundorf, P., 1987, Nature, 330, 728.
- Bernatowicz et al. 2006, Meteorites and the Early Solar System II, D. S. Lauretta and H. Y. McSween Jr. (eds.), University of Arizona Press, Tucson, 943 pp., p.109-126.
- Chan, S. J., & Kwok, S. 1990, A&A, 237, 354.
- Cherchneff, I., 2006, A&A, 456, 1001.
- Chigai, T., Yamamoto, T. 2003, Geochim. Cosmochim. Acta., 67, 64.
- Clayton, D.D., Nittler, L.R., 2004, ARA&A, 42, 39.
- Clément, D., Mutschke, H., Klein, R., & Henning, T. 2003, ApJ, 594, 642
- Clément, D., Mutschke, H., Klein, R., & Henning, T. 2005, ApJ, 621, 985.

- Comelli, G. Stohr, J., Robinson, C.J., Jark, W. (1988) *Phys. Rev. B* 38, 7511.
- Corman, A.B., Speck, A.K., Volk, K., Sloan, G.C., Barlow, M.J., 2008, in prep.
- Daulton et al. 2003, *GeCoA*, 67, 4743.
- DePew, K., Speck, A.K., Dijkstra, C., 2006, *ApJ*, 640, 971.
- de Graauw, T. et al. 1996, *A&A*, 315, 49.
- Dijkstra, C., Speck, A. K., Reid, R.B., Abraham, P., 2005, *ApJ*, 633, L133.
- Dijkstra, C., Speck, A. K., 2006, *ApJ* 651, 288.
- Dominik, Sedlmayr, & Gail, 1989, *A&A*, 223, 227.
- Draine, B.T., Lee, H.M. 1984, *ApJ*, 285, 89.
- Fong, D., Meixner, M., Shah, R., 2003, *ApJ*, 582, L39.
- Forrest, W. J.; Houck, J. R.; McCarthy, J. F., 1981, *ApJ*, 248, 195.
- Friedman, C. 1969, *Physica* 41, 189.
- Gilman, R. C. 1969, *ApJ*, 155, L185.
- Gilra, D. P., & Code, A. D. 1971, *BAAS*, 3, 379.
- Goebel, J. H., Cheeseman, P., & Gerbault, F. 1995, *ApJ*, 449, 246.
- Goebel, J. H., Moseley, S.H., 1985, *ApJ*, 290, L35.
- Griffin, I.P., 1990 *MNRAS*, 247, 591.
- Groenewegen, M.A.T. 1994, *A&A*, 290, 207.
- Groenewegen, M.A.T. 1995, *A&A*, 293, 463.
- Groenewegen, M.A.T. 1996, *A&A*, 305, 475.
- Groenewegen, M.A.T. 1997, *Ap&SS*, 251, 89.
- Groenewegen, M.A.T. et al. 1998, *MNRAS*, 293, 18.
- Groenewegen, M.A.T. et al. 1999, *A&AS*, 140, 197.
- Groenewegen, M. A. T., Sevenster, M., Spoon, H. W. W., Pérez, I., 2002, *A&A*, 390, 511.

- Hackwell, J. A. 1972, *A&A*, 21, 239.
- Hanner, M. S. 1988, *Infrared Observations of Comets Halley and Wilson and Properties of the Grains*, ed. M. S. Hanner (NASA C-3004; Washington: NASA), 22.
- Hildebrand, R.H., 1983, *QJRAS*, 24, 267.
- Hony et al. 2003 *A&A*, 402, 211.
- Hony, S., Waters, L.B.F.M., Tielens, A.G.G.M, 2002, *A&A*, 390, 533
- Huggins, P.J., Olofsson, H., Johansson, L.E.B., 1988, *ApJ*, 332, 1009.
- Iben, I., Jr. & Renzini, A. 1983, *ARA&A*, 21, 271.
- Ivezic, Z. & Elitzur, M. 1995, *ApJ*, 445, 415.
- Ivezic, Z. & Elitzur, M. 1997, *MNRAS*, 287, 799.
- Jennings, C. L., Savina, M. R., Messenger, S., Amari, S., Nichols, R. H., Pellin, M. J., Podosek, F. A. 2002, *LPSC*, 33, A1833
- Jones, B., Merrill, K. M., Puetter, R. C., & Willner, S. P. 1978, *AJ*, 83, 1437
- Jørgensen, U. G., Hron, J., Loidl, R., 2000, *A&A*, 356, 253.
- Jura, M., Turner, J. L., Van Dyk, S., Knapp, G. R., 2000, *ApJ*528, L105.
- Jura, M. 1994, *ApJ*, 434, 713.
- Kelires, P.C., 1993, *Phys. Rev. B* 47, 1829.
- Kessler, M.F. et al., 1996, *A&A*, 315, L27
- Kim, S.-H., Martin, P. G., Hendry, P.D., 1994, *ApJ*, 422, 164.
- Knapp, G.R., Morris, M., 1982, *ApJ*, 292, 640.
- Lagadec, E. et al., 2007, *MNRAS*, 376, 1270.
- Lagadec, E. et al., 2008, *MNRAS*, 383, 399.
- Lagadec, E., Zijlstra, A.A. , 2008, *MNRAS*, in press.
- Lambert, D.L., Gustafsson, B., Eriksson, K., Hinkle, K.H., 1986, *ApJS*, 62, 373.

- Leech, K., et al. 2003, The ISO Handbook, Vol. V. SWS - The Short Wavelength Spectrometer Version 2.0.1 (June, 2003). Series edited by T.G. Mueller, J.A.D.L. Blommaert, and P. Garcia-Lario. ESA SP-1262, (Noordwijk: ESA).
- Leisenring, J. M., Kemper, F., Sloan, G. C., 2008, ApJ, 681, 1557.
- Lodders, K., Fegley, B., 1995, Meteoritics, 30, 661.
- Lodders, K., Fegley, B., 1999, Asymptotic Giant Branch Stars, IAU Symposium 191, Edited by T. Le Bertre, A. Lebre, and C. Waelkens. p. 279
- Loup, C., Forveille, T., Omont, A., Paul, J. F., 1993, A&AS, 99, 291.
- Mathis, J. S., Rumpl, W., & Nordsieck, K. H. 1977, ApJ217, 425.
- Martin, P.G., Rogers, C., 1987, ApJ, 322, 374.
- Meixner, M., Zalucha, A., Ueta, T., Fong, D., Justtanont, K., 2004, ApJ, 614, 371.
- Meixner, M., Ueta, T., Bobrowsky, M., Speck, A., 2002, ApJ, 571, 936.
- 1999, ApJS, 122, 221.
- Nenkova, M., Ivezić, Z., & Elitzur, M. 2000 in ASP Conf. Ser. 196, Thermal Emission Spectroscopy and Analysis of Dust, Disks, and Regoliths, ed. M. L. Sitko, A.L. Sprague & D. K. Lynch (San Francisco: ASP), 77.
- Neugebauer, G. et al. 1984, Science, 224, 1.
- Nuth, J.A., et al. 1985, ApJ, 290, L41.
- Olofsson, H., Eriksson, K., Gustafsson, B., Carlstroem, U. 1993a, ApJS, 87, 267.
- Olofsson, H., Eriksson, K., Gustafsson, B., Carlstroem, U. 1993b, ApJS, 87, 305.
- Omont et al. 1993, A&A, 267, 515.
- Omont, A. et al., 1995, ApJ, 454, 819
- Pégourié, B. 1988, A&A, 194, 335.
- Pitman, K.M., Speck, A.K., Hofmeister, A.M., 2006, MNRAS, 371, 1744.
- Pitman, K.M., Speck, A.K., Hofmeister, A.M., 2008, A&A, 483, 661.
- Prombo, C.A., Podosek, F.A., Amari, S., Lewis, R. S. 1993, ApJ, 410, 393.

- Renzini, A, 1981, in *Physical Processes in Red Giants*, eds. I. Iben Jr. & A. Renzini, Reidel:Dordrecht, pp431.
- Roawn-Robinson, M., Harris, S., 1983, *MNRAS*, 202, 797.
- Rouleau, F., Martin, P.G., 1991, *ApJ*, 377, 526.
- Saada, D., 2000, Ph.D. thesis
- Sahai, R., 2004, in *ASP Conf. Ser. 313, Asymmetrical Planetary Nebulae III: Winds, Structure and the Thunderbird*, ed. M. Meixner et al. (San Francisco: ASP) 141.
- Sharp, C.M., Wasserburg, G.J., 1995, *GeCoA*, 59, 1445.
- Skinner C.J., et al., 1997, *A&A*, 328, 290.
- Skinner, C.J., Meixner, M., Bobrowsky, M., 1998, *MNRAS*, 300, L29.
- Skrutskie, M. F., Reber, T. J., Murphy, N. W., Weinberg, M. D., 2001, *BAAS*, 33, 1437.
- Sloan, G.C., et al. 2006, *ApJ*, 645, 1118.
- Sloan, G. C., Little-Marenin, I. R., & Price, S. D. 1998, *AJ*, 115, 809.
- Soker, N., Subag, E. 2005, *AJ*, 130, 2717.
- Speck, A. K., Barlow, M. J., & Skinner, C. J. 1997, *MNRAS*, 288, 431.
- Speck, A. K., Hofmeister, A.M., & Barlow, M. J., 1999, *ApJ*, 513, L87.
- Speck, A. K., Barlow, M. J., Sylvester, R.J & Hofmeister A.M., 2000, *A&AS*, 146, 437.
- Speck, A. K., Thompson, G. D., & Hofmeister, A. M. 2005, *ApJ*, 634, 426.
- Speck, A. K., Cami, J., Markwick-Kemper, C., Leisenring, J., Szczerba, R., Dijkstra, C., Van Dyk, S. & Meixner, M. 2006, *ApJ*, 650, 892.
- Szczerba, R., Omont, A., Volk, K., Cox, P., Kwok, S., 1997, *A&A*, 317, 859.
- Thompson, G.D., Corman, A.B., Speck, A.K., Dijkstra, ., 2006, *ApJ*, 652, 1654.
- Treffers, R., & Cohen, M. 1974, *ApJ*, 188, 545.
- van der Veen, W. E. C. J., Habing, H. J., 1988, *A&A*, 194, 125.
- Vassiliadis, E., Wood, P.R., (VW) 1993, *ApJ*, 413, 641.

- Villaver, E., Manchado, A., Garcia-Segura, G., 2002a, *ApJ*, 581, 1204.
- Villaver, E., Manchado, A., Garcia-Segura, G., 2002b, *ApJ*, 571, 880.
- Virag, A. et al., 1992 *Geochim. Cosmochim. Acta*, 56, 1715.
- Volk, K., Kwok, S., & Langill, P. 1992, *ApJ*, 391, 285.
- Volk, K., Xiong, G., & Kwok, S. 2000, *ApJ*, 530, 408.
- Vassiliadis, E. & Wood, P. R. 1993, *ApJ*, 413, 641.
- Waelkens, C., Waters, L. B. F. M. 1999, in *IAU Symp. 191, Asymptotic Giant Branch Stars*, ed. T. le Bertre, A. Lbre & C. Waelkens (San Francisco: ASP), 519.
- Woitke, P., 2006, *A&A*, 452, 537.
- Wood, P.R., et al. 1992, *ApJ*, 397, 552.
- Zijlstra, A., et al. , 2006, *MNRAS*, 370, 1961.

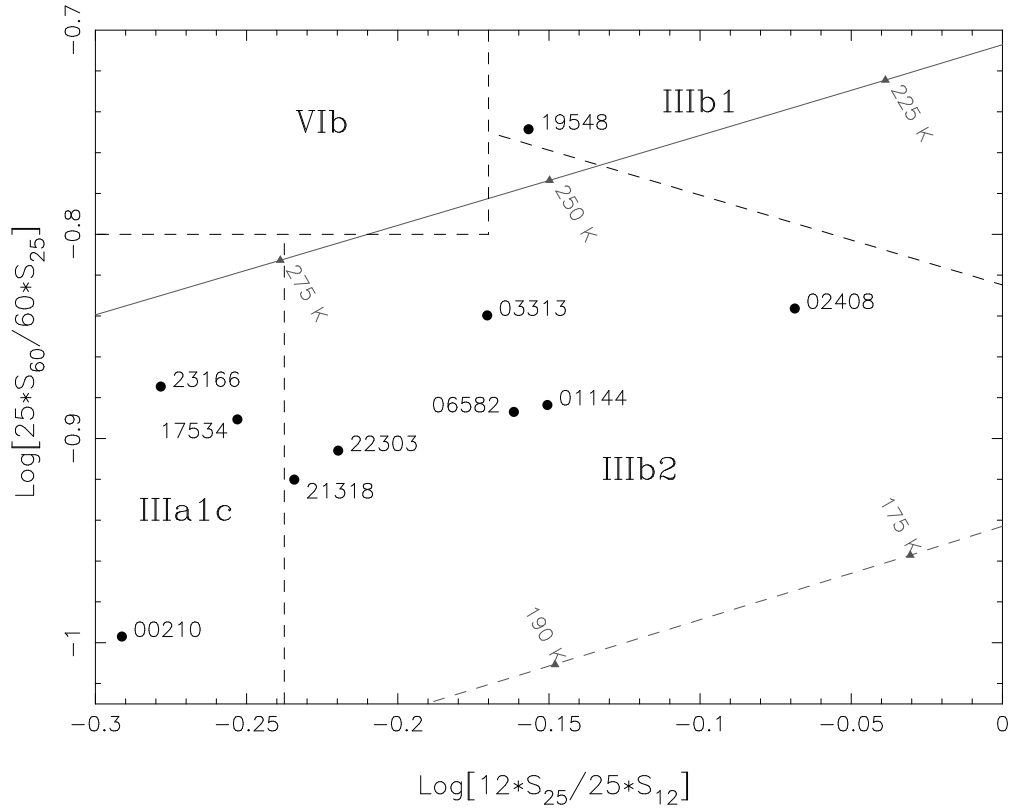


Fig. 1.— Regions in the IRAS color-color diagram populated by extreme carbon stars. see text for details. The black body curve is indicated by the solid grey line. The modified blackbody [$B(T, \lambda) * \lambda^{-1}$] is indicated by the dashed grey line

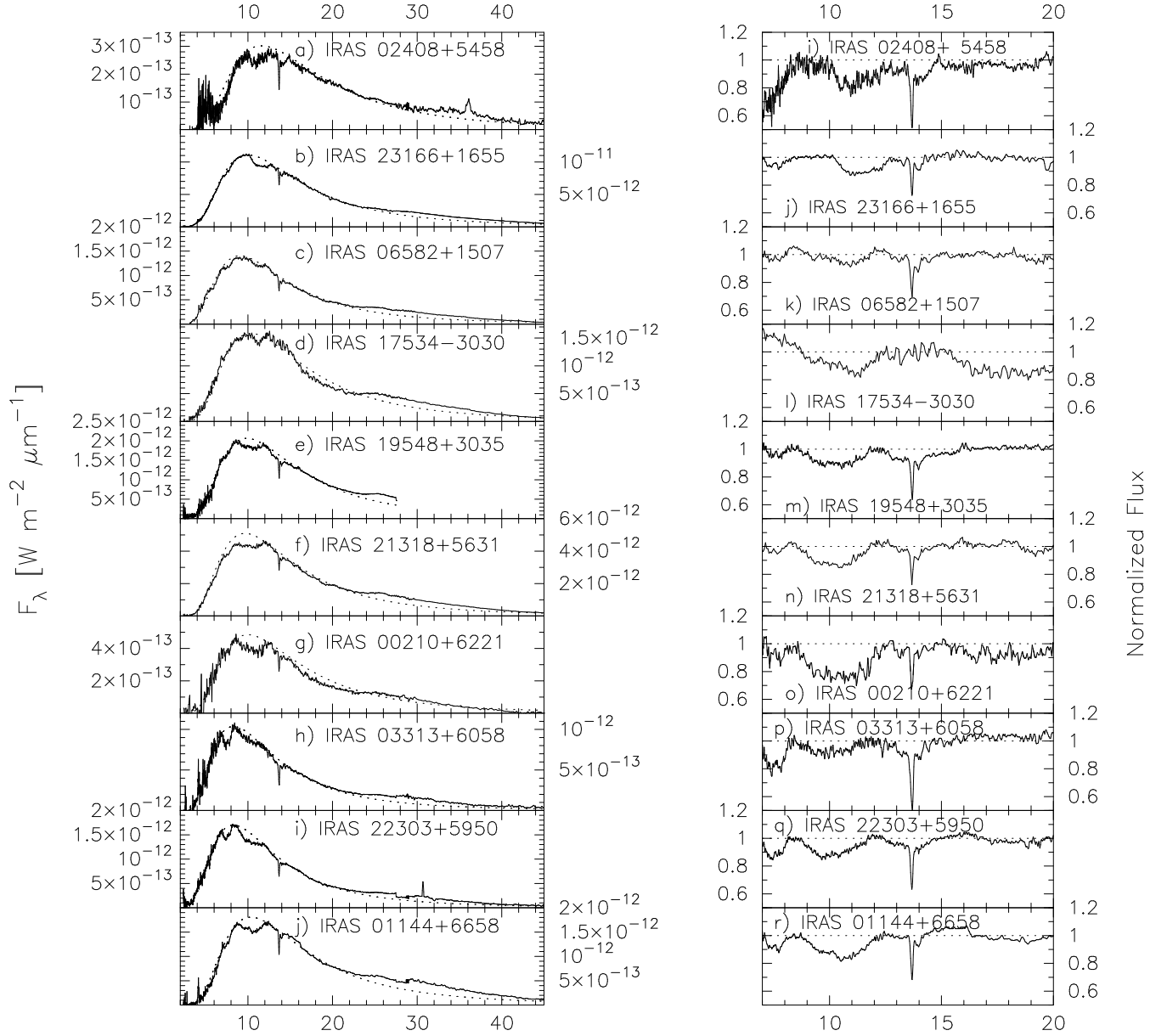


Fig. 2.— *ISO* SWS spectra of ten extreme C-stars. *Left Panel*: Flux-calibrated spectra and fitted blackbody continua. Solid line = *ISO* spectrum; dashed line = best-fitting blackbody continuum; The y -axis is the flux (F_λ) in $\text{W m}^{-2} \mu\text{m}^{-1}$; the x -axis is wavelength in μm . *Right Panel*: Continuum-divided spectra. Table 3 lists the blackbody temperatures used in each case to produce the continuum and the continuum-divided spectra.

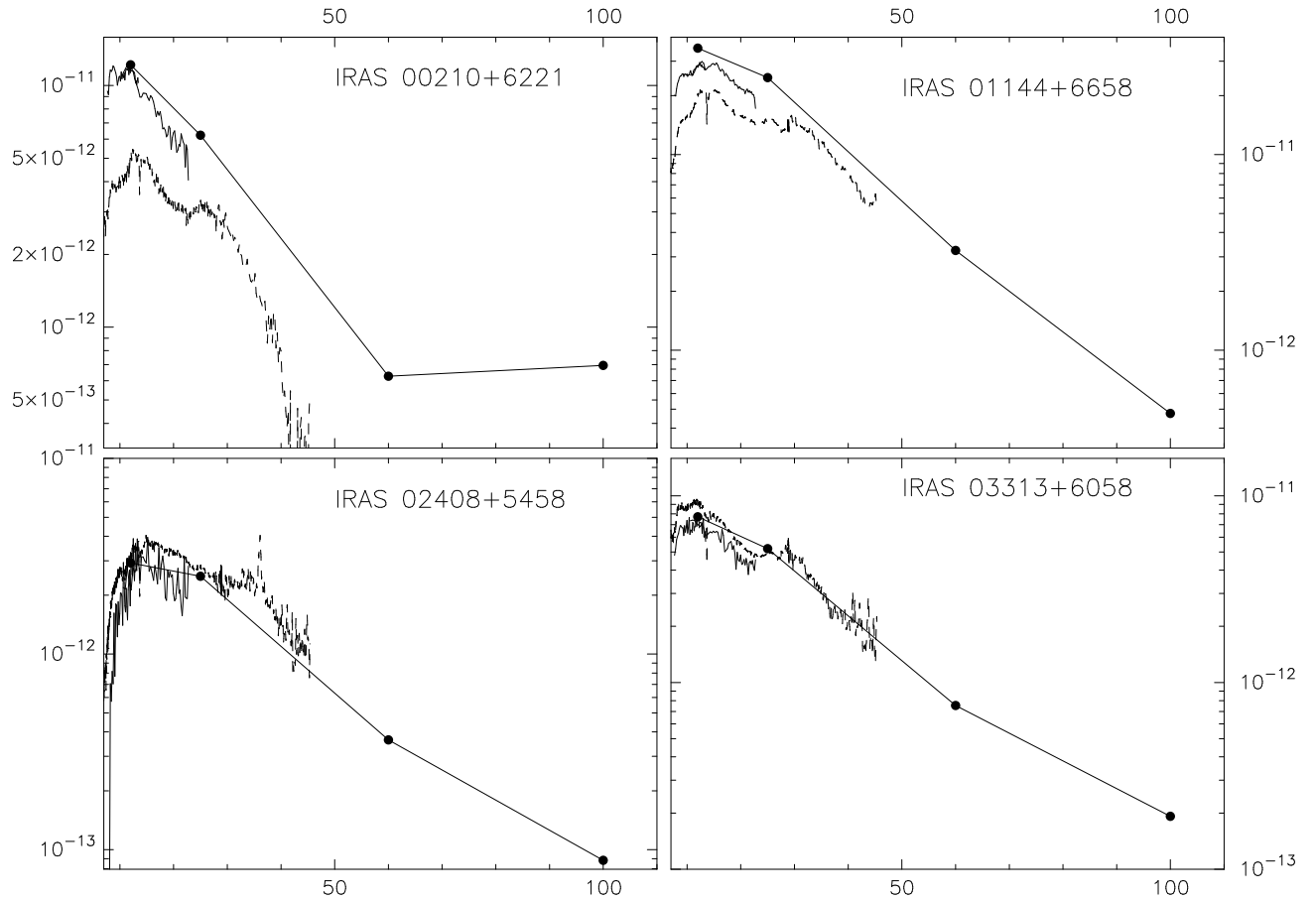


Fig. 3.— *ISO* SWS spectra of sample extreme C-stars together with *IRAS* 12, 25, 60 and $100\mu\text{m}$ photometry points and *IRAS* LRS spectra. Solid line = *IRAS* spectrum; points = *IRAS* photometry points; dashed line = *ISO* SWS spectrum. The y -axis is the flux (λF_λ) in W m^{-2} ; the x -axis is wavelength in μm .

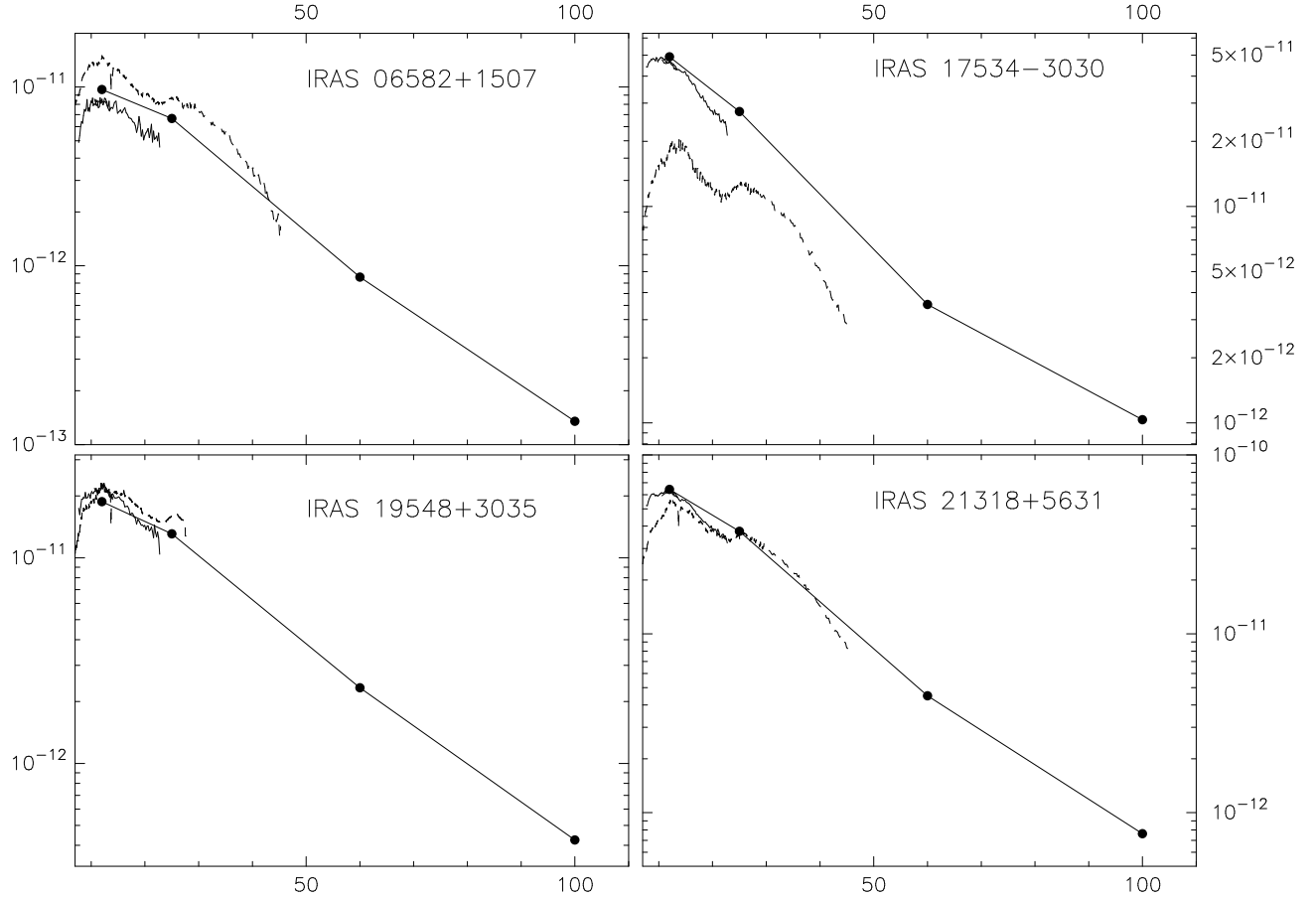


Fig. 4.— *ISO* SWS spectra of sample extreme C-stars together with *IRAS* 12, 25, 60 and $100\mu\text{m}$ photometry points and *IRAS* LRS spectra (part 2). Solid line = *IRAS* spectrum; points = *IRAS* photometry points; dashed line = *ISO* SWS spectrum. The y -axis is the flux (λF_λ) in W m^{-2} ; the x -axis is wavelength in μm .

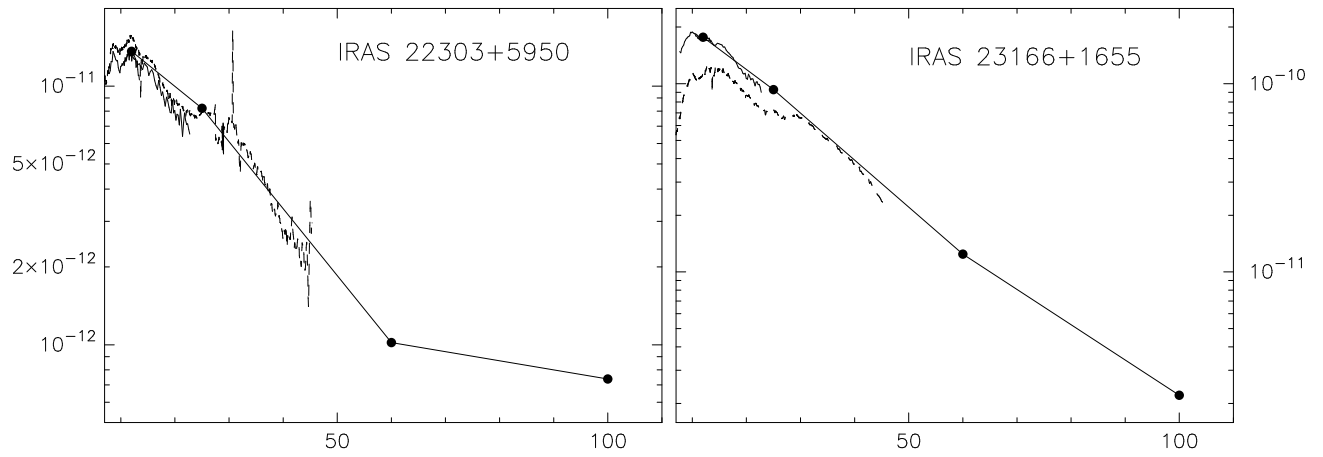


Fig. 5.— *ISO* SWS spectra of sample extreme C-stars together with *IRAS* 12, 25, 60 and $100\mu\text{m}$ photometry points and *IRAS* LRS spectra (part 3). Solid line = *IRAS* spectrum; points = *IRAS* photometry points; dashed line = *ISO* SWS spectrum. The y -axis is the flux (λF_λ) in W m^{-2} ; the x -axis is wavelength in μm .

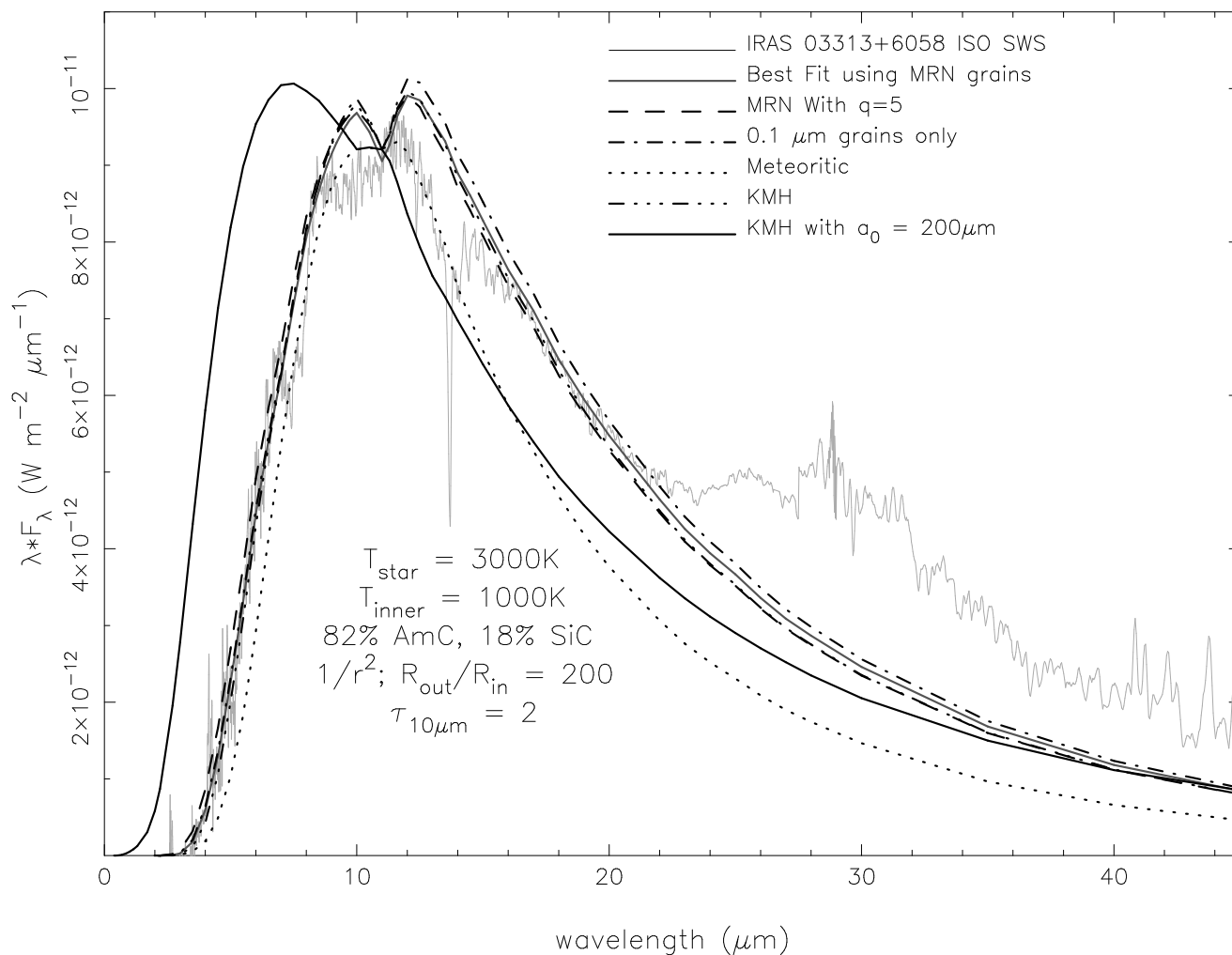


Fig. 6.— The effect of grain-size distributions on the model spectral energy distribution. In all cases the model parameters are identical except for the grain-size distribution. see § 3.2 for detailed description of the grain-size distributions. The grey line shows the ISO-SWS spectrum of IRAS03313+6058 for comparison.

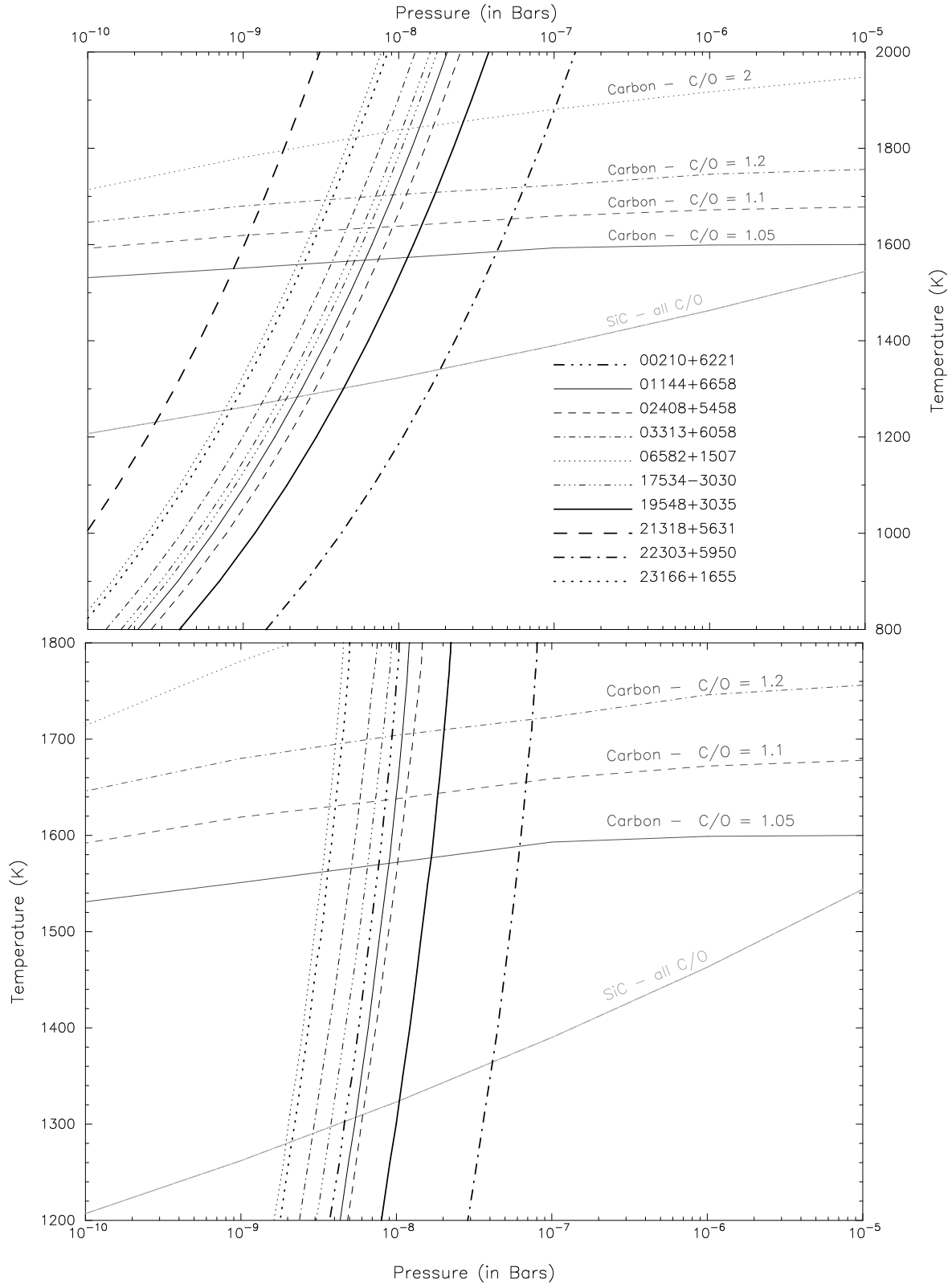


Fig. 7.— Pressure-Temperature space for the dust condensation region around extreme carbon stars (assumes solar metallicity). Grey lines indicate the condensation temperature for a given pressure as calculated by Lodders & Fegley (1995). Black lines indicate the P–T paths for the outflowing gas from our sample stars; (*top*) as calculated from the published CO mass-loss rates and expansion velocities (see § 3.4.2 for details); and (*bottom*) as calculated

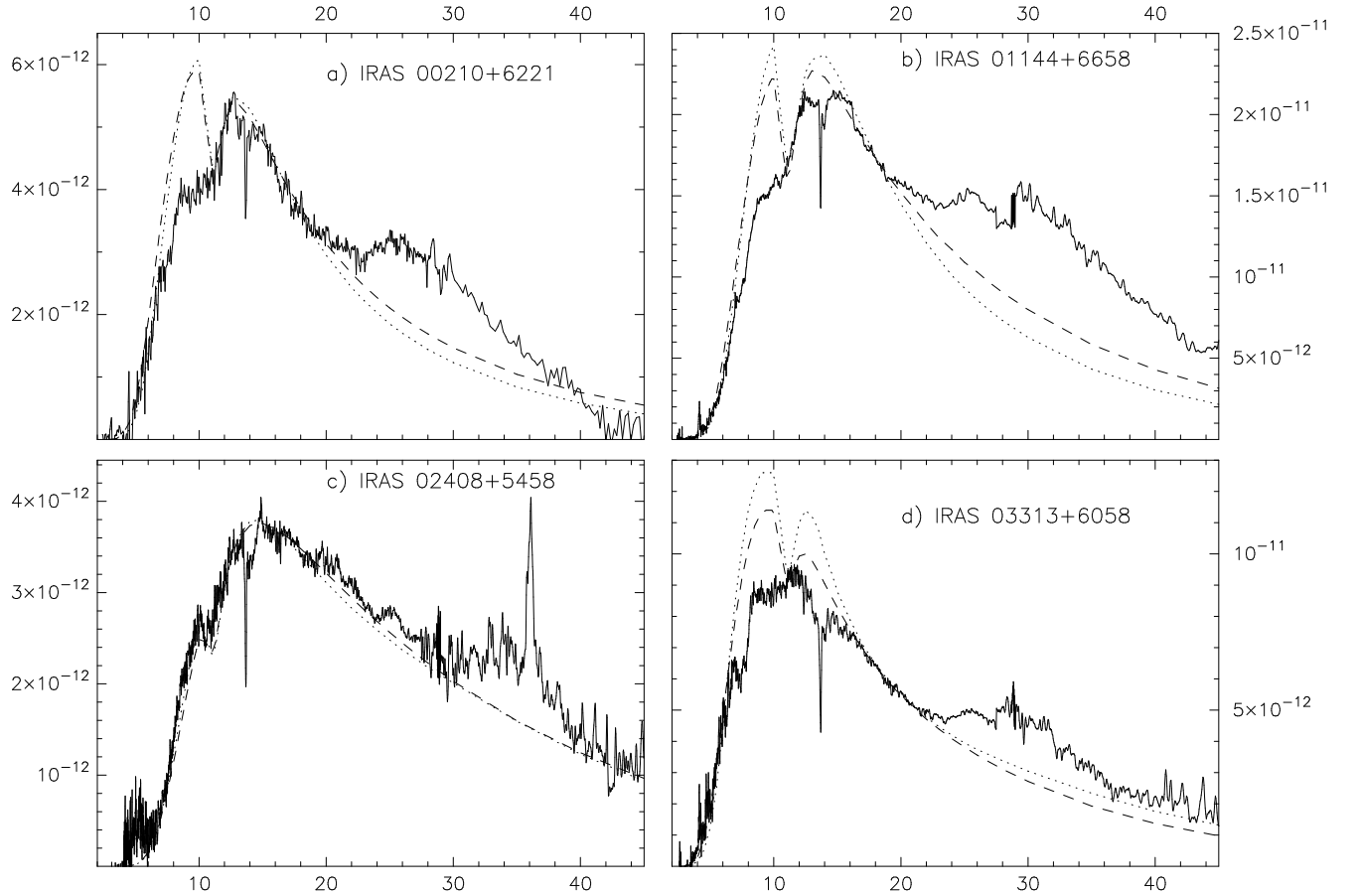


Fig. 8.— Best fit models (part 1). solid line = ISO-SWS spectrum; dashed line = best fit model using MRN grain-size distribution; dotted line = best fit model using “meteoritic” grain-size distribution; X -axis is wavelength (μm); y -axis is flux (λF_λ) in W m^{-2} . In all cases, $T_\star=3000\text{ K}$ and $T_{\text{inner}}=1800\text{ K}$. Model parameters are listed in Table 5

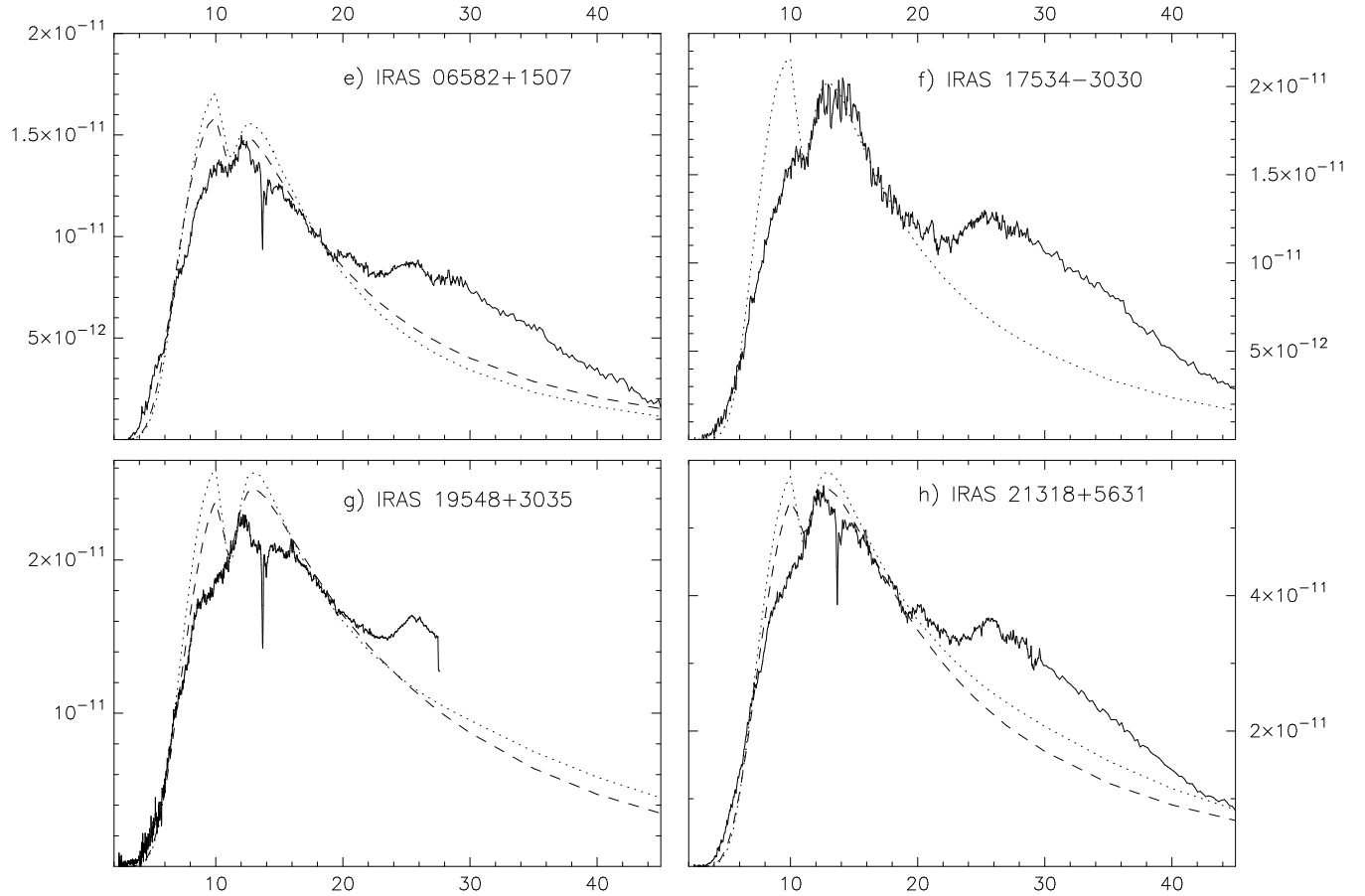


Fig. 9.— Best fit models (part 2) solid line = ISO-SWS spectrum; dashed line = best fit model x -axis is wavelength (μm); y -axis is flux (λF_λ) in W m^{-2} . In all cases, $T_\star=3000\text{ K}$ and $T_{\text{inner}}=1800\text{ K}$. Model parameters are listed in Table 5

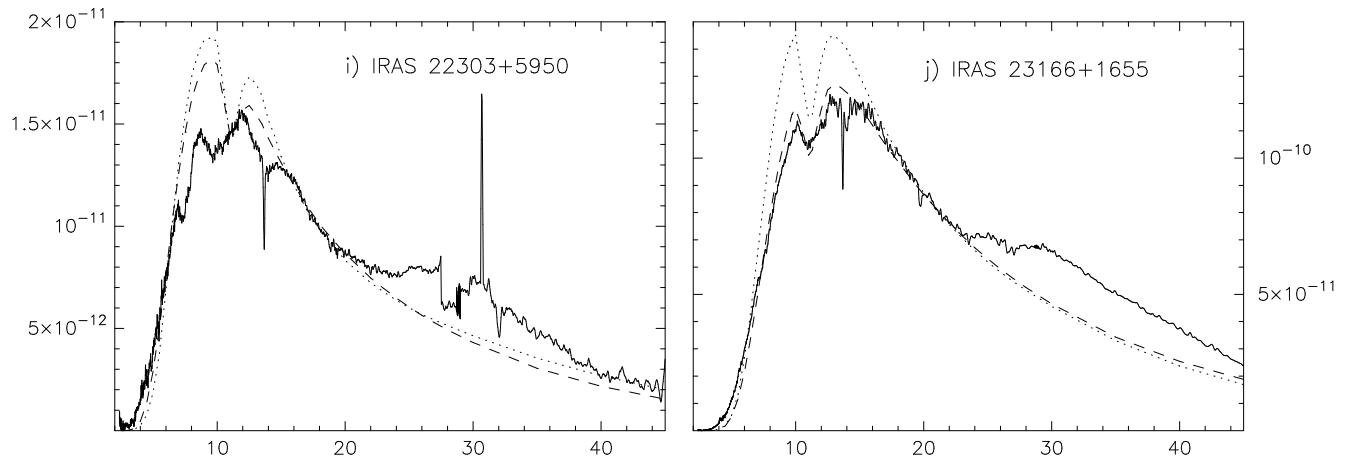


Fig. 10.— Best fit models (part 3) solid line = ISO-SWS spectrum; dashed line = best fit model x -axis is wavelength (μm); y -axis is flux (λF_λ) in W m^{-2} . In all cases, $T_\star=3000$ K and $T_{\text{inner}}=1800$ K. other parameters are indicated in the legend. Parameters of these models are also listed in Table 5

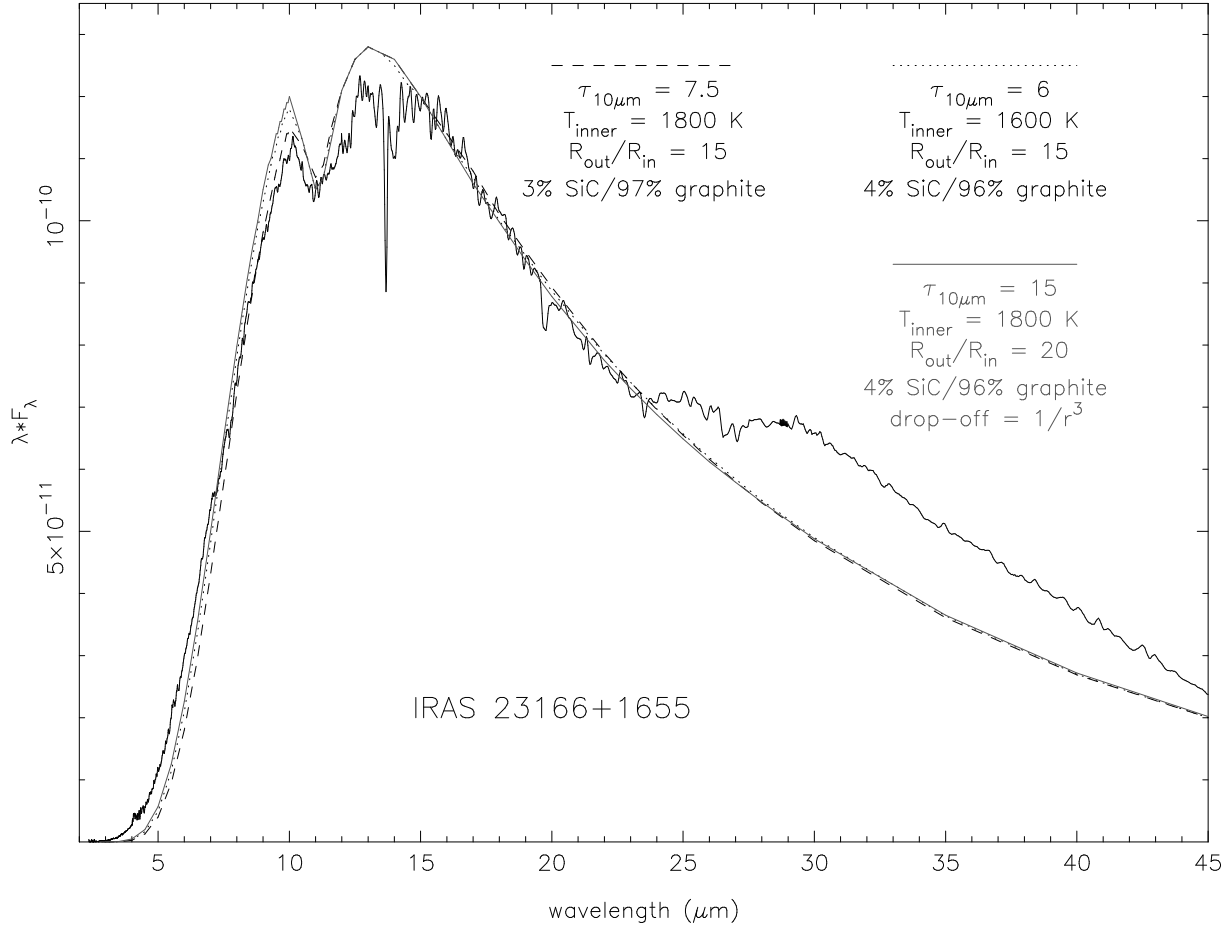


Fig. 11.— Degeneracy in the best fit models for IRAS 23166+1655. solid line = ISO-SWS spectrum; dashed line = best fit model with $T_{\text{inner}}=1800 \text{ K}$ dotted line = best fit model with $T_{\text{inner}}=1600 \text{ K}$ X-axis is wavelength (μm); y-axis is flux (λF_{λ}) in W m^{-2} . In both cases, $T_{\star}=3000 \text{ K}$ other parameters are indicated in the legend.

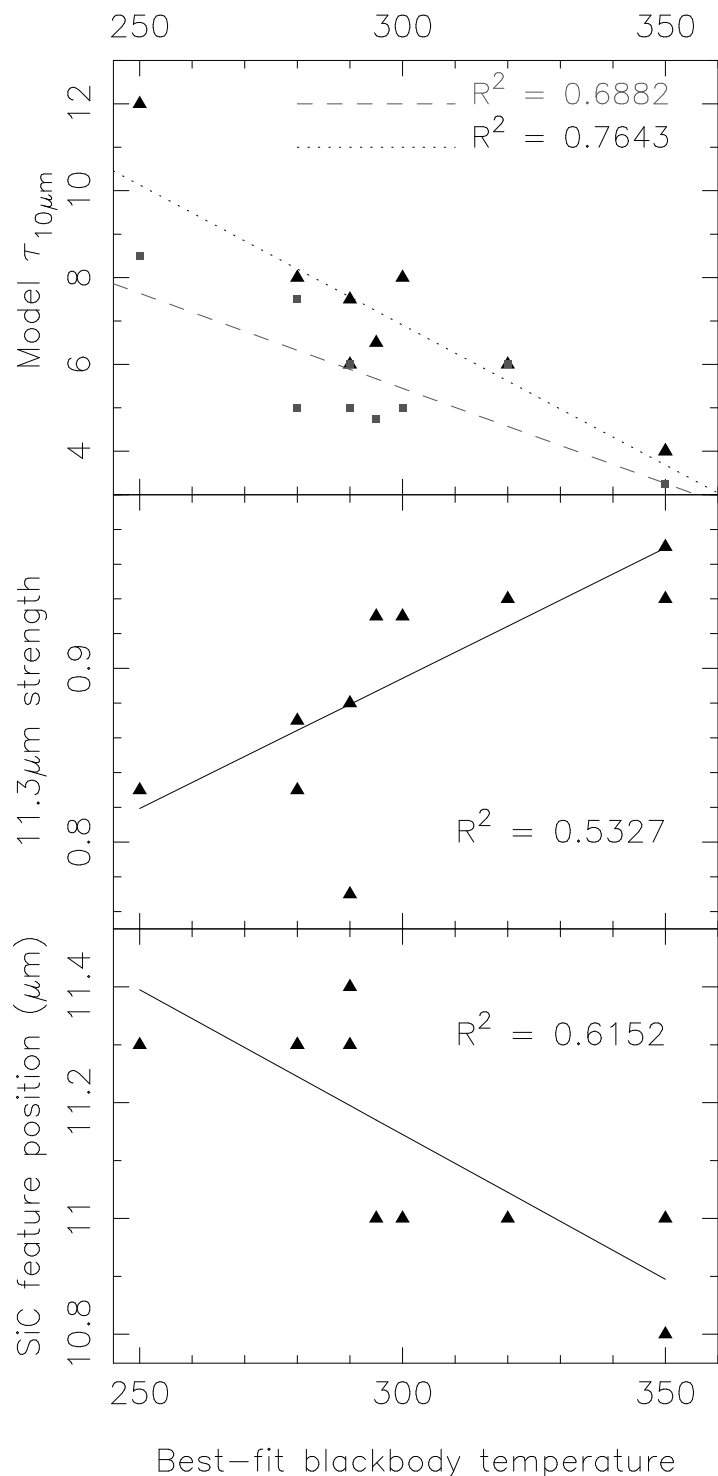


Fig. 12.— Correlations between the best-fit blackbody temperature and (*top*) modeled optical depth; (*middle*) 11.3 μm feature-to-continuum ratio; and (*bottom*) SiC feature position. Solid lines represent the linear regression fit through the points. In the top figure, the dotted line represents the linear regression for model fits with MRN grainsize distributions. Grey points are for meteoritic grainsize models, and grey dashed line is the linear regression fit through the points.

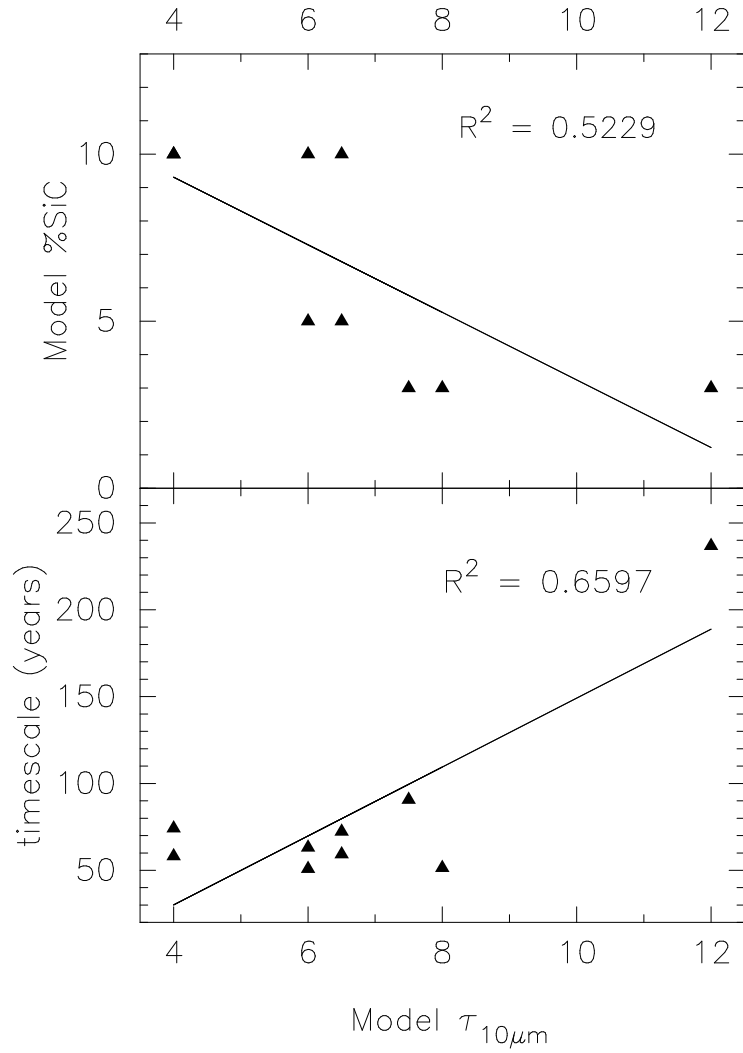


Fig. 13.— Correlations between the modeled optical depth and (*top*) the modeled %age SiC (*bottom*) the calculated superwind timescale from Table 6. Solid lines represent the linear regression fit through the points.

Table 1: Previous Models of Extreme Carbon stars with $11\mu\text{m}$ absorption features

Star	composition [†] (SiC%)	Grain-size (μm)	$\tau_{11.3\mu\text{m}}$	drop-off	R_{in}^* ($\times 10^{-4}$ pc)	T_{in} (K)	\dot{M}^* $M_{\odot} \text{yr}^{-1}$	REF
00210+6221	0	0.1	4.5	3.00	0.362/D	1000	$12 \times 10^{-5}/D$	2
01144+6658	8	0.1	4.84			1000	9.50×10^{-7}	4
06582-1507	0	...	5.15			1000	1.08×10^{-4}	1
	0	0.1	2.1	2.25	1.23	1000	2.59×10^{-4}	2
17534–3030	0	0.1	4.4	2.50	1.39	1000	8.20×10^{-4}	2
19548+3035	0	0.1	2.5	2.50	1.17	1000	3.89×10^{-4}	2
21318+5631	0	...	1.36			700	1.10×10^{-4}	3
23166+1655	0	0.1	1.12			650	5.50×10^{-7}	4
	30	...	7.85			1000	3.30×10^{-5}	1
	0	...	1.19			650	1.00×10^{-4}	3

References 1: Volk et al. (1992); 2: Volk et al. (2000); 3: Groenewegen (1995); 4: Groenewegen et al. (1998)

* originally quoted as a function of distance. Value quoted here assume distances from Groenewegen et al. (2002), listed in Table 4

† composition assumes remainder dust is carbon. In all but Volk et al. (1992) the carbon is amorphous; Volk et al. (1992) uses graphitic carbon.

Neither Volk et al. (1992) nor Groenewegen (1995) specify the grains sizes used in their models

Table 2: Target List

IRAS Number	Other Names	R.A. ⁸ (J2000)	Decl. (J2000)	TDT number	Date of Observation
00210+6221	CGCS 6006	00 23 51.2	+62 38 16.4	40401901	1996 Dec 24
01144+6658	V829 Cas, AFGL 190, CGCS 6017	01 17 51.6	+67 13 55.4	68800128	1997 Oct 03
02408+5458		02 44 25.2	+55 11 15	80002504	1998 Jan 24
03313+6058	CGCS 6061	03 35 30.7	+61 08 47.2	62301907	1997 Jul 31
06582+1507	CGCS 6193	07 01 08.44	+15 03 39.8	71002102	1997 Oct 26
17534–3030	AFGL 5416, CGCS 6690	17 56 33.1	–30 30 47.1	12102004	1996 Mar 17
19548+3035	AFGL 2477, CGCS 6851	21 50 45.0	+53 15 28.0	56100849	1997 May 30
21318+5631	AFGL 5625S, CGCS 6888	21 33 22.98	+56 44 35.0	11101103	1997 Mar 7
22303+5950	CGCS 6906	22 32 12.8	+60 06 04.1	77900836	1998 Jan 02
23166+1655	LL Peg, AFGL 3068, CGCS 6913	23 19 12.39	+17 11 35.4	37900867	1996 Nov 29

Table 3: Observed parameters of the target sources

IRAS Number	T_{BB} (K)	Feature Barycenter	Feature ¹ Strength	FWHM	Equivalent Width	9.7 μm^2 Strength	11.3 μm^3 Strength	SiC ⁴ position
00210+6221	290K	10.45	0.73	2.28	0.60	0.76	0.77	11.3
01144+6658	280K	10.51	0.82	2.32	0.35	0.88	0.87	11.3
02408+5458	250K	11.28	0.73	2.20	0.30	—	0.83	11.3
03313+6058	350K	10.12	0.87	1.72	0.17	0.90	0.97	10.8
06582+1507	320K	10.25	0.91	0.70	0.1	0.97	0.94	11.0
17534–3030	280K	10.59	0.87	0.80	0.30	0.92	0.83	11.3
19548+3035	295K	10.24	0.87	2.39	0.25	0.88	0.93	11.0
21318+5631	300K	10.20	0.84	2.90	0.37	0.88	0.93	11.0
22303+5950	350K	10.25	0.84	1.70	0.25	0.86	0.94	11.0
23166+1655	290K	11.42	0.86	2.00	0.21	—	0.88	11.4

¹ Feature strength is the “peak”-to-continuum ratio and is measured and the barycentric position.

² The 9.7 μm strength is the feature-to-continuum ratio measured at 9.7 μm .

³ The 11.3 μm strength is the feature-to-continuum ratio measured at 11.3 μm .

⁴ The SiC position, the the approximate barycentric position that the SiC feature would have if the short wavelength side of the absorption were due to silicate 9.7 μm absorption.

Table 4: Compilation of CO mass-loss rates and expansion velocities, together with distances and luminosities of sample stars.

Source Name	v_{exp} km/s	D kpc	\dot{M}_{gas} $M_{\odot} \text{ yr}^{-1}$	\dot{M}_{dust} $M_{\odot} \text{ yr}^{-1}$	L_{\star} L_{\odot}
00210+6221*	16.7	3.97	3.02×10^{-5}	—	1×10^4
01144+6658	18	2.78	6.38×10^{-5}	1.51×10^{-7}	1.69×10^4
02408+5458*	11	5.3	1.60×10^{-5}	3.5×10^{-7}	5.70×10^3
03313+6058	13.9	5.24	2.37×10^{-5}	1.14×10^{-7}	1.31×10^4
06582+1507	13.7	4.7	1.43×10^{-5}	1.07×10^{-7}	1.32×10^4
17534–3030	19	2	3.76×10^{-5}	1.06×10^{-7}	1.21×10^4
19548+3035	22.3	3.38	1.14×10^{-4}	2.15×10^{-7}	1.32×10^4
21318+5631	19.6	1.77	7.69×10^{-6}	1.18×10^{-7}	1.24×10^4
22303+5950	18.3	3.86	3.19×10^{-4}	1.09×10^{-7}	1.25×10^4
23166+1655	15.1	1	1.44×10^{-5}	8.27×10^{-8}	1.10×10^4

All data are from Groenewegen et al. (2002) except those marked with *. IRAS 02408+5458 data come from Groenewegen et al. (1999). IRAS 00210+6221 data are compiled from Volk et al. (2000) (\dot{M} , which also convolves the distance from Groenewegen et al. 2002); and Volk et al. (1992) (v_{exp}).

Table 5: Model and Derived Parameters

IRAS Number	T_{\star}	T_{inner}	$R_{\text{out}}/R_{\text{in}}$	$\tau_{10\mu\text{m}}$	Composition	
					SiC%	Graphite %
MRN grain size distribution						
00210+6221	3000	1800	10	6	10	90
01144+6658	3000	1800	15	6.5	10	90
02408+5458	3000	1800	20	12	3	97
03313+6058	3000	1800	15	4	10	90
06582+1507	3000	1800	10	6	5	95
17534-3030	3000	1800				
19548+3035	3000	1800	15	6.5	5	95
21318+5631	3000	1800	10	8	3	97
22303+5950	3000	1800	15	4	10	90
23166+1655	3000	1800	15	7.5	3	97
Meteoritic grain size distribution						
00210+6221	3000	1800	10	6	30	70
01144+6658	3000	1800	10	7.5	30	70
02408+5458	3000	1800	100	8.5	12	88
03313+6058	3000	1800	500	3.25	40	60
06582+1507	3000	1800	10	6	20	80
17534-3030	3000	1800	20	5	35	65
19548+3035	3000	1800	100*	4.75	25	75
21318+5631	3000	1800	100	5	20	80
22303+5950	3000	1800	500	3.25	40	60
23166+1655	3000	1800	50	5	25	75

* Models with $R_{\text{out}}/R_{\text{in}} > 100$ can be accommodated because the data beyond $26\mu\text{m}$ is poor and ignored, but based on the similarity of this source to IRAS 21318+5631, we assume this is a good upper limit.

Table 6: Size and age of the dust shells

IRAS Number	MRN size distribution			Meteoritic size distribution		
	R_{in} (10^{14}cm)	R_{out} (10^{14}cm)	Age (yrs)	R_{in} (10^{14}cm)	R_{out} (10^{14}cm)	Age (yrs)
00210	2.68	26.8	50.9	2.78	2.78	52.8
01144	2.74	41.1	72.4	3.08	30.8	54.2
02408	4.11	82.2	236.8	2.99	299	861.3
03313	2.17	32.6	74.2	2.10	1050	2393.7
06582	2.73	27.3	63.1	2.72	27.2	62.9
17534	2.51	50.2	83.7	2.51	50.2	83.7
19548	2.78	41.7	59.3	2.38	238	338.2
21318	3.18	31.8	51.4	2.41	241	389.6
22303	2.24	33.6	58.2	2.10	1050	1818.2
23166	2.88	43.2	90.7	2.45	123	257.1

Calculation of R_{out} is based on the model parameters listed in Table 5. R_{in} comes from the model output. The calculation of the age of the dust shells is then done using these data and the observed expansion velocities listed in Table 4